Check for updates

Advanced Materials

ADVANCED MATERIALS
www.advmat.de

RESEARCH ARTICLE OPEN ACCESS

Engineering Tunable Helper Lipid Architecture to Improve Messenger RNA Lipid Nanoparticle Performance

Shrirang Karve[1] | Neha Kaushal[1] | Hanming Zhang[1] | Chetan Poojari[2] | Dipen Parande[1] | Saket Dolare[1] | Lingyun Liu[1] | Zhongyu Li[1] | Trent P. Northen[1] | Jackie Tang[1] | Jae-Heon Kim[1] | Mengwei Sun[1] | Ana Kume[1] | Krishna Chaitanya Suddala[1] | Chung Li Wu[1] | Allison Dauner[3] | Danielle McCulley[3] | Alex Shumate[3] | David Forgacs[3] | Ranjitha Uppala[3] | Jose Salvatico[3] | Rose Jolicoeur[3] | Heesik Yoon[3] | Ramesh Dasari[1] | Saswata Karmakar[1] | Zhen Hu[1] | Ashish Sarode[1] | Amita Vaidya[1] | Younan Ma[1] | Aurélie Deliot[4] | Solene Bechelli[1] | Michael Rieger[2] | Anusha Dias[1] | Sudha Chivukula[1] | Brian Schanen[3] | Hongfeng Deng[1] | Frank DeRosa[1] | Regis Gervier[1]

[1]mRNA Center of Excellence, Sanofi, Waltham, Massachusetts, USA | [2]mRNA Center of Excellence, Sanofi, Marcy-L'Étoile, France | [3]mRNA Center of Excellence, Sanofi, Orlando, Florida, USA | [4]VCDS Department, Sanofi Pasteur, Marcy-L'Étoile, France

Correspondence: Shrirang Karve (shri.karve@sanofi.com) | Hongfeng Deng (hongfeng.deng@sanofi.com)

Received: 14 August 2026 | **Revised:** 2 November 2026 | **Accepted:** 6 November 2026

Keywords: chemistry | computational biology | immunogenicity | linker | lipid based nanoparticles | messenger RNA | molecular dynamics | nanoparticle | RNAi therapeutics

ABSTRACT

Helper lipids are essential structural components of lipid nanoparticles (LNPs), yet systematic design principles linking helper lipid architecture to messenger RNA (mRNA) delivery performance remain poorly defined. Here we identify helper lipid architecture as a major, largely unexplored design lever for optimizing LNP performance. Using a modular library of more than 80 rationally designed helper lipids, we show that systematic variation in headgroup chemistry, linker topology, and tail cardinality reshapes both LNP biophysical behavior and biological performance. Martini molecular dynamics (MD) simulations combined with multimodal structural analyses reveal that high-performing scaffolds undergo a pH-dependent transition into fusogenic inverse hexagonal-like ordering, substantially lowering the energetic barrier for endosomal escape. These performance gains persist across the clinically relevant ALC-0315 and DLin-MC3-DMA platforms, establishing helper lipid architecture as a transferable design parameter across distinct ionizable lipid chemistries. Translating these design principles into function, optimized helper lipid formulations restore hepatic protein expression in a mouse model of ornithine transcarbamylase (OTC) deficiency and increase antigen expression and immunogenicity in both preclinical models and in the in vitro human MIMIC platform. Together, these findings establish helper lipids as tunable molecular actuators of potency, tolerability, and stability, offering an engineering framework for next-generation mRNA vaccines and therapeutics.

Shrirang Karve and Neha Kaushal contributed equally to this work.

This is an open access article under the terms of the Creative Commons Attribution-NonCommercial-NoDerivs License, which permits use and distribution in any medium, provided the original work is properly cited, the use is non-commercial and no modifications or adaptations are made. All other rights reserved, including rights for text and data mining and training of artificial intelligence technologies or similar technologies.
© 2026 The Author(s). *Advanced Materials published* by Wiley-VCH GmbH

1 | Introduction

The development of lipid nanoparticles (LNPs) for messenger RNA (mRNA) delivery has redefined modern medicine, transforming a niche area of nucleic acid research into a programmable modality for vaccines and therapeutics [1–3]. The success of SARS-CoV-2 vaccines reinforced the critical role of LNPs in prophylaxis, while also rapidly ushering in a "post-vaccine" era of precision medicine [4, 5]. This shift encompasses complex applications such as protein replacement therapy for rare genetic disorders [6], in vivo cell reprogramming [7], and CRISPR-based genome editing [8]. Unlike viral vectors, the LNP platform offers a modular, nonintegrating system capable of restoring or rewriting cellular function at the transcriptomic level. The standard LNP architecture comprises a four-component system: an ionizable lipid, a zwitterionic phospholipid, cholesterol, and a PEGylated lipid [9]. Historically, the ionizable lipid has been regarded as the primary functional "workhorse" [10], with engineering efforts focused almost exclusively on its iterative refinement [11, 12]. However, as clinical targets expand, it is increasingly evident that efficacy and organ-tropism are governed by the synergistic interplay of all lipid components [13, 14]. Zwitterionic phospholipids, traditionally referred to as "helper lipids", exert a disproportionate influence on internal morphology, stability, and endosomal escape kinetics. Current clinical phospholipid benchmarks, such as DSPC (1,2-distearoyl-sn-glycero-3-phosphocholine) and DOPE (1,2-dioleoyl-sn-glycero-3-phosphoethanolamine), illustrate a "stability-potency paradox", where DSPC-based formulations offer high structural integrity but limited fusogenicity, while DOPE-based systems enhance pH-dependent membrane disruption at the cost of formulation stability [15–17]. Decoupling these requirements necessitates moving beyond the traditional binary choice. A major challenge in the field is the identification of design principles that remain effective across different ionizable lipid chemistries and therapeutic applications. Here, we sought to determine whether helper lipid architecture could serve as an orthogonal and transferable design parameter for mRNA delivery. While substantial efforts have focused on the optimization of ionizable lipids, recent studies [18, 19] have highlighted the importance of helper lipid composition and pH-dependent phase behavior in regulating LNP structure, membrane interactions, and intracellular delivery. Nevertheless, a systematic understanding of how helper lipid architecture governs these properties and whether transferable design rules can be established across diverse helper lipid chemotypes remains limited.

To this end, we systematically explored helper lipid design space through rational architectural diversification aimed at improving LNP performance. We sought to redefine the helper lipid landscape by designing and synthesizing a library of over 80 novel helper lipids (HLs) spanning three distinct scaffolds. This library explored a multidimensional design space encompassing variations in amine headgroup substitution, hydrophobic tail number (two-tailed glycerol versus three-tailed structures derived from citric acid or pentaerythritol cores), linker length, and tail branching architecture, while maintaining a fixed formulation background consisting of ionizable lipid A, cholesterol, and DMG-PEG. Top candidates were identified through in vivo screening of human erythropoietin (hEPO) mRNA-LNP formulations administered intramuscularly and intravenously, respectively. In the context of prophylactic vaccination, LNPs incorporating these engineered scaffolds significantly augmented immunogenicity, eliciting superior neutralizing antibody titers against influenza hemagglutinin compared to standard DSPC- or DOPE-containing formulations. Furthermore, to assess translational utility beyond murine models, we utilized the human cell-based MIMIC (*Modular IMmune* In vitro *Construct*) platform [20], enabling high-fidelity evaluation of innate and adaptive immune responses in a human-predictive environment [21]. Simultaneously, we identified a class of three-tailed helper lipids that demonstrated a marked propensity for hepatic delivery, effectively rescuing the phenotype of urea cycle dysfunction in a disease-relevant model of ornithine transcarbamylase (OTC) deficiency [22–24]. To provide a rigorous mechanistic bridge between lipid geometry and biological function, we further employed coarse-grained Martini molecular dynamics (MD) simulations to systematically evaluate stalk formation energetics (ΔG) and membrane-mixing kinetics of these novel architectures [25, 26]. By integrating biophysical modeling, human-cell-based immune profiling, and in vivo therapeutic evaluation, we demonstrate that structural innovation within the helper lipid architecture provides a broadly applicable solution to the tripartite barriers of delivery efficiency, stability, and tolerability. Our findings establish a robust design rationale for multi-functional LNPs, providing a modular toolkit for the next generation of vaccines, therapeutics, and genomic medicines.

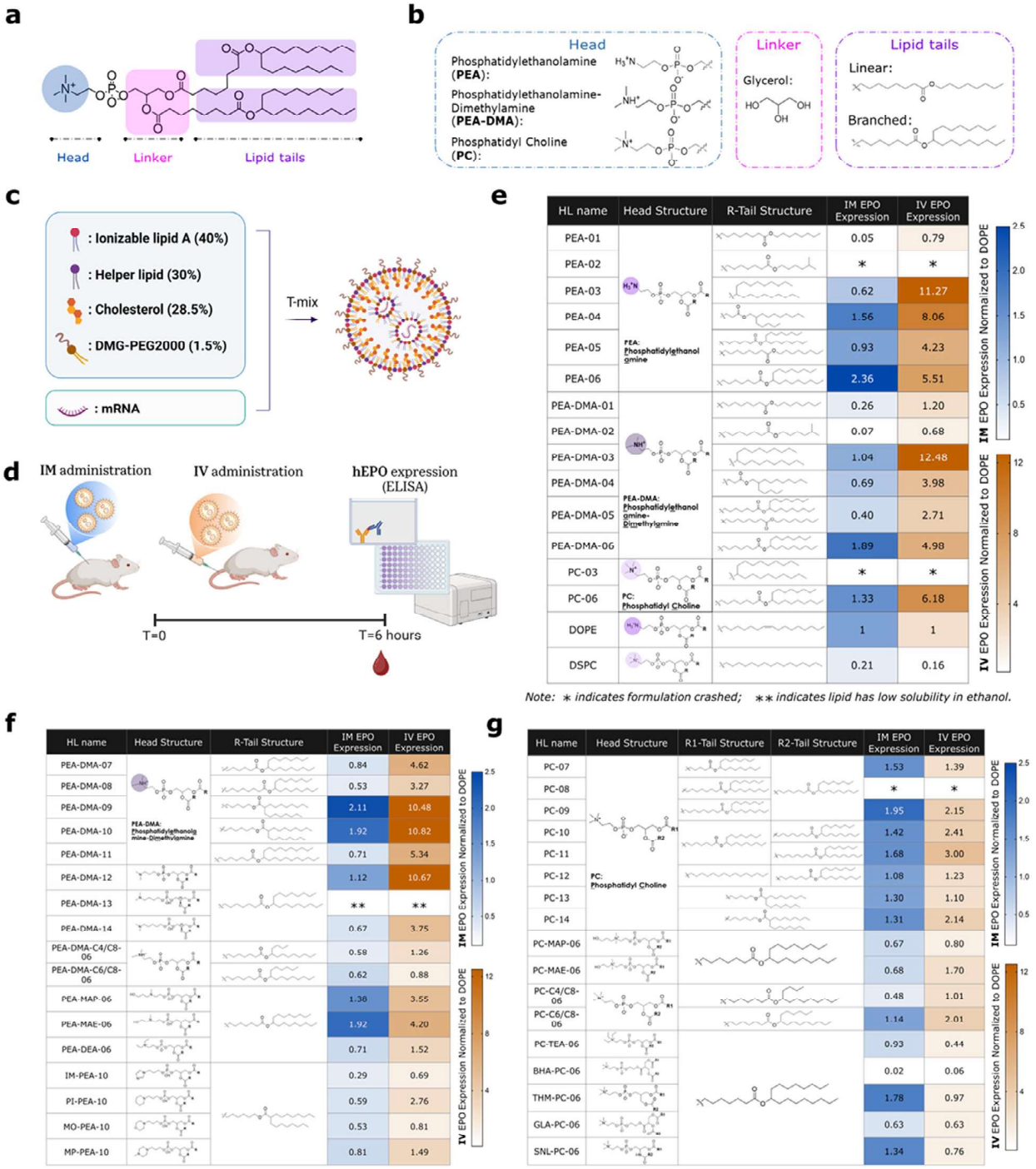
2 | Results and Discussion

2.1 | A Modular Helper Lipid Toolkit for Precision Engineering of mRNA-Lipid Nanoparticles

To rigorously define the design space for next-generation helper lipids (HLs)s, we engineered a modular library centered on a glycerol backbone, systematically varying headgroup substitution and hydrophobic tail architecture (Figure 1a; Representative synthesis schemes are shown in Figure S1, and abbreviations are listed in Table S1). Three headgroups, PEA (primary amine), PEA-DMA (tertiary amine), and PC (quaternary amine), representing a gradient of amine substitution (Figure 1b) were evaluated. These were coupled with six distinct tail scaffolds (Tails 01 – 06) designed to test the impact of branching and biodegradable ester linkages on mRNA delivery. This matrix was formulated into LNPs (with the other three components—ionizable lipid A, cholesterol, and DMG-PEG—held constant) encapsulating hEPO mRNA [27] (Figure 1c). Our initial assessment aimed to identify novel helper lipids that outperform DOPE across both intramuscular (IM) and intravenous (IV) routes of administration. To increase the sensitivity of this screen, the standard LNP composition used in Figures 1 and 2 incorporates the helper lipid at 30 mol%. At this ratio, DOPE markedly enhances endosomal escape and cytosolic delivery, as demonstrated in our previous optimization studies [27, 28], and thus provides a stringent, high-performing benchmark for comparison.

When normalized to the standard DOPE formulation, the results revealed a distinct expression landscape (Figure 1e). DSPC exhibited significantly diminished expression (0.2-fold), while

15214095, 0, Downloaded from https://advanced.onlinelibrary.wiley.com/doi/10.1002/adma.75746, Wiley Online Library on [17/11/2026]. See the Terms and Conditions (https://onlinelibrary.wiley.com/terms-and-conditions) on Wiley Online Library for rules of use; OA articles are governed by the applicable Creative Commons License



HL name	Head Structure	R-Tail Structure	IM EPO Expression	IV EPO Expression
PEA-01	PEA: Phosphatidylethanolamine		0.05	0.79
PEA-02			*	*
PEA-03			0.62	11.27
PEA-04			1.56	8.06
PEA-05			0.93	4.23
PEA-06			2.36	5.51
PEA-DMA-01	PEA-DMA: Phosphatidylethanolamine-Dimethylamine		0.26	1.20
PEA-DMA-02			0.07	0.68
PEA-DMA-03			1.04	12.48
PEA-DMA-04			0.69	3.98
PEA-DMA-05			0.40	2.71
PEA-DMA-06			1.89	4.98
PC-03	PC: Phosphatidyl Choline		*	*
PC-06			1.33	6.18
DOPE			1	1
DSPC			0.21	0.16

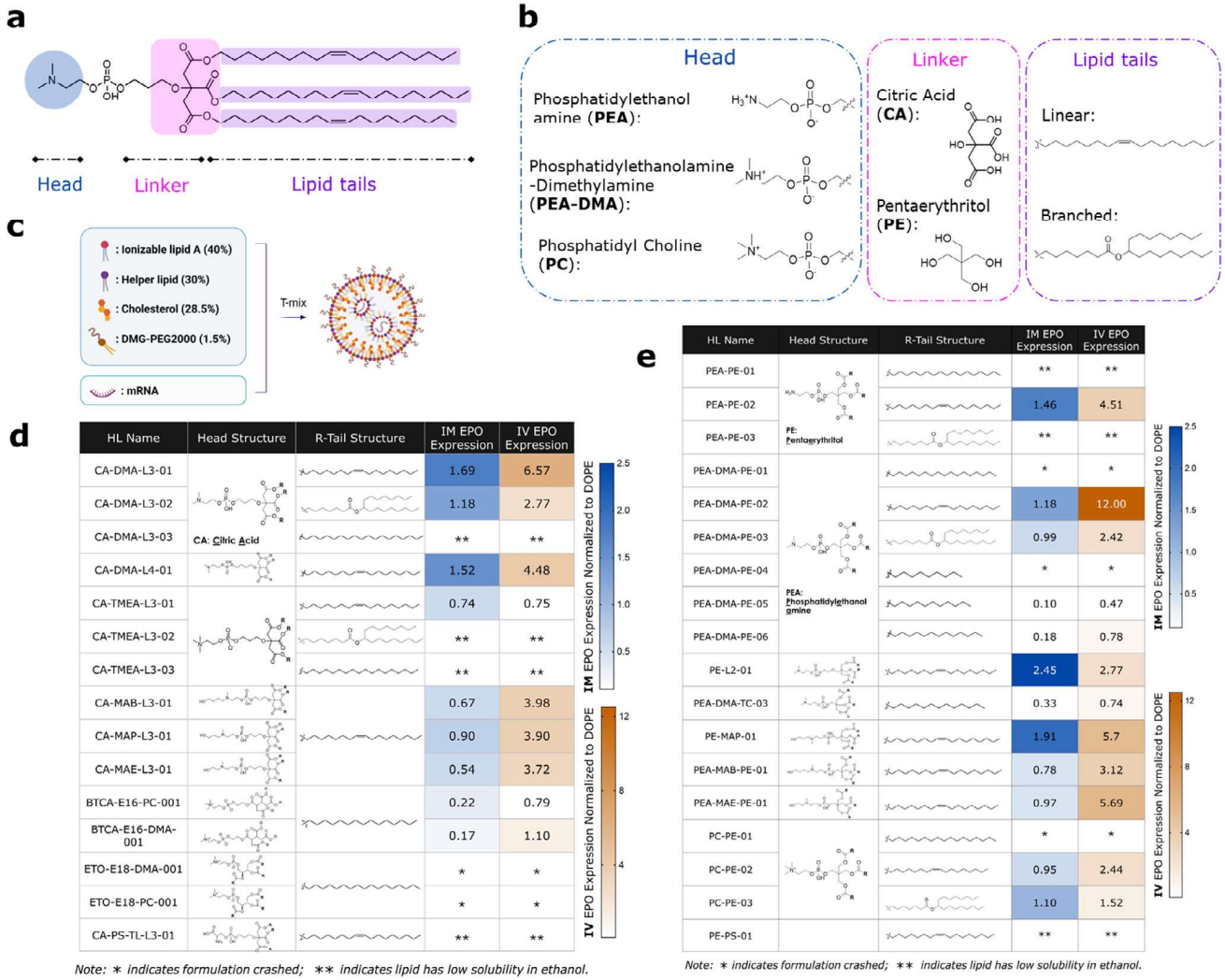
*Note: * indicates formulation crashed; ** indicates lipid has low solubility in ethanol.*

HL name	Head Structure	R-Tail Structure	IM EPO Expression	IV EPO Expression
PEA-DMA-07	PEA-DMA: Phosphatidylethanolamine-Dimethylamine		0.84	4.62
PEA-DMA-08			0.53	3.27
PEA-DMA-09			2.11	10.48
PEA-DMA-10			1.92	10.82
PEA-DMA-11			0.71	5.34
PEA-DMA-12			1.12	10.67
PEA-DMA-13			**	**
PEA-DMA-14			0.67	3.75
PEA-DMA-C4/C8-06			0.58	1.26
PEA-DMA-C6/C8-06			0.62	0.88
PEA-MAP-06			1.38	3.55
PEA-MAE-06			1.92	4.20
PEA-DEA-06			0.71	1.52
IM-PEA-10			0.29	0.69
PI-PEA-10			0.59	2.76
MO-PEA-10			0.53	0.81
MP-PEA-10			0.81	1.49

HL name	Head Structure	R1-Tail Structure	R2-Tail Structure	IM EPO Expression	IV EPO Expression
PC-07	PC: Phosphatidyl Choline			1.53	1.39
PC-08				*	*
PC-09				1.95	2.15
PC-10				1.42	2.41
PC-11				1.68	3.00
PC-12				1.08	1.23
PC-13				1.30	1.10
PC-14				1.31	2.14
PC-MAP-06				0.67	0.80
PC-MAE-06				0.68	1.70
PC-C4/C8-06				0.48	1.01
PC-C6/C8-06				1.14	2.01
PC-TEA-06				0.93	0.44
BHA-PC-06				0.02	0.06
THM-PC-06				1.78	0.97
GLA-PC-06				0.63	0.63
SNL-PC-06				1.34	0.76

FIGURE 1 | Overview of rational design and screening of novel two-tailed helper lipids for enhanced mRNA delivery. (a, b) Modular chemical space of novel two-tailed helper lipid (HL) library. The scaffolds are defined by four structural domains: varied headgroup chemistries including Phosphatidylethanolamine (PEA), Phosphatidylethanolamine-Dimethylamine (PEA-DMA), and Phosphatidyl Choline (PC), connected via glyceride-based linker to linear or branched lipid tails. (c) Schematic of the LNP screening composition utilizing a four-component system (Ionizable Lipid A: HL: Cholesterol: DMG-PEG2000) that encapsulate hEPO mRNA. (d) in vivo LNP screening strategy. hEPO-encoding mRNA was encapsulated in LNPs containing novel HLs and administered to mice via intramuscular (IM) or intravenous (IV) injection to quantify local and systemic expression, respectively. hEPO expression was determined after 6 h via ELISA. (e-g) Heatmaps summarizing the structure-activity relationship (SAR) of the two-tailed HL library. LNP delivery efficiency is measured as hEPO expression normalized to the standard DOPE helper lipid for both IM (blue) and IV (orange) routes. The library includes initial screening leads and iterative designs based on PEA-DMA-06 and PC-06 architecture. Asterisk (*) denotes LNP formulations that either failed during self-assembly or (**) precluded formulation due to limited lipid solubility. Female BALB/c mice (6-8 weeks old) were intramuscularly or intravenously injected with LNPs loaded with hEPO mRNA at a dose of 0.1 μg per mouse or 0.017 mg/kg, respectively. All data are presented as the mean fold change over DOPE controls ($n = 4$).

15214095, 0, Downloaded from https://advanced.onlinelibrary.wiley.com/doi/10.1002/adma.75746, Wiley Online Library on [17/11/2026]. See the Terms and Conditions (https://onlinelibrary.wiley.com/terms-and-conditions) on Wiley Online Library for rules of use; OA articles are governed by the applicable Creative Commons License



HL Name	Head Structure	R-Tail Structure	IM EPO Expression	IV EPO Expression
CA-DMA-L3-01	CA: Citric Acid		1.69	6.57
CA-DMA-L3-02			1.18	2.77
CA-DMA-L3-03			**	**
CA-DMA-L4-01			1.52	4.48
CA-TMEA-L3-01			0.74	0.75
CA-TMEA-L3-02			**	**
CA-TMEA-L3-03			**	**
CA-MAB-L3-01			0.67	3.98
CA-MAP-L3-01			0.90	3.90
CA-MAE-L3-01			0.54	3.72
BTCA-E16-PC-001			0.22	0.79
BTCA-E16-DMA-001			0.17	1.10
ETO-E18-DMA-001			*	*
ETO-E18-PC-001			*	*
CA-PS-TL-L3-01			**	**

HL Name	Head Structure	R-Tail Structure	IM EPO Expression	IV EPO Expression
PEA-PE-01	PE: Pentaerythritol		**	**
PEA-PE-02			1.46	4.51
PEA-PE-03			**	**
PEA-DMA-PE-01	PEA: Phosphatidylethanolamine		*	*
PEA-DMA-PE-02			1.18	12.00
PEA-DMA-PE-03			0.99	2.42
PEA-DMA-PE-04			*	*
PEA-DMA-PE-05			0.10	0.47
PEA-DMA-PE-06			0.18	0.78
PE-L2-01			2.45	2.77
PEA-DMA-TC-03			0.33	0.74
PE-MAP-01			1.91	5.7
PEA-MAB-PE-01			0.78	3.12
PEA-MAE-PE-01			0.97	5.69
PC-PE-01			*	*
PC-PE-02			0.95	2.44
PC-PE-03			1.10	1.52
PE-PS-01			**	**

FIGURE 2 | Rational design and structure activity mapping of novel three-tailed helper lipid library. (a-b) Modular engineering of three-tailed helper lipid (HL) structures utilizing citric acid (CA) and pentaerythritol (PE) backbones as cores for design of these lipids. The design space integrates varied headgroup chemistries, including PEA, PEA-DMA, and PC coupled with diverse linker lengths and R-tail configurations. (c) Schematic of the LNP composition utilizing a four-component system (Ionizable Lipid A: HL: Cholesterol: DMG-PEG2000) for the encapsulation of hEPO mRNA. (d, e) Comprehensive heatmaps illustrating the structure–activity relationships (SAR) for CA-based and PE-based three-tailed HLs. Delivery efficacy is quantified as hEPO protein expression normalized to the standard DOPE following IM (blue) and IV (orange) administration. Notably, PEA-DMA-PE-02 and CA-DMA-L3-01 demonstrate exceptional systemic hEPO protein expression, achieving up to 12-fold and 6.57-fold increases in IV expression relative to DOPE, respectively. Asterisks (*) denote formulations that exhibited instability during assembly or (**) limited solubility. Female BALB/c mice (6-8 weeks old) were injected with LNPs loaded with hEPO mRNA at a dose of 0.1 μg per mouse via intramuscular route or 0.017 mg/kg via intravenous route. All data are presented as the mean fold change over DOPE ($n = 4$).

PEA- and PEA-DMA-based helper lipids incorporating branched or asymmetrical tails (03–06) consistently matched or exceeded DOPE-based LNPs via both IM and IV routes. Guided by these findings, we extended the 06-tail architecture to the quaternary PC series, where PC-06 emerged as a lead candidate. While maintaining parity with DOPE following IM administration, PC-06 demonstrated significantly improved potency after IV delivery. Notably, the 06-tail scaffold consistently supported superior hEPO expression across both routes, independent of headgroup composition.

To further explore the nuances of the 06-tail architecture, we synthesized analogues 07–11 to systematically probe the influence of ester orientation and chain length (Figure 1f). Among these, the reverse-ester isomers (09 and 10) emerged as highly potent, eliciting a 10-fold increase in intravenous expression relative to DOPE-formulated LNPs. Parallel optimization of the PEA-DMA headgroup via alkyl spacer modulation identified PEA-DMA-12 (three-carbon spacer) as a lead candidate, achieving 10-fold gains in expression (Figure 1f). While an expansive screen of alternative headgroups including methyl aminopropanol (MAP), methyl aminoethanol (MAE), diethyl amine (DEA), and various heterocycles consistently outperformed DOPE, none reached the peak performance of PEA-DMA-12. This underscores the high structural specificity required between the headgroup and hydrophobic domain to achieve optimal systemic delivery. Comparison across the PC series confirmed that, while tail variations improved performance, none surpassed PC-06, suggesting that

15214095, 0, Downloaded from https://advanced.onlinelibrary.wiley.com/doi/10.1002/adma.75746, Wiley Online Library on [17/11/2026]. See the Terms and Conditions (https://onlinelibrary.wiley.com/terms-and-conditions) on Wiley Online Library for rules of use; OA articles are governed by the applicable Creative Commons License

the 06 architecture provides a superior hydrophobic foundation that requires specific polar pairing for maximal efficacy (Figure 1g).

Building on these insights, we extended our design rationale to three-tailed scaffolds centered on citric acid and pentaerythritol cores to increase the number of tails (Figure 2a,b). In the citric acid series, tail unsaturation (CA-DMA-L3-01) provided encouraging expression gains, whereas saturated-tail variants and quaternary PC derivatives suffered from physicochemical instability (Figure 2d). To merge high tail cardinality with different connectivity, we engineered a modular pentaerythritol-derived core (Figure 2e). This platform allowed for the systematic evaluation of saturated, unsaturated, and branched ester motifs. The integration of these features identified PEA-DMA-PE-02, a triunsaturated tertiary amine scaffold, as one of the lead candidates, achieving a 12-fold enhancement in hEPO expression relative to DOPE via IV administration. A basic characterization panel for formulations is presented in Figure S2. Zeta potential measurements reported in Figure S2e-h were obtained in 1 mM KCl, a low ionic strength medium commonly used for electrophoretic mobility measurements. To assess particle charge under more physiologically relevant conditions, representative formulations were additionally evaluated in 0.1X PBS (Figure S2i), where all formulations exhibited near-neutral zeta potentials (+1.8 to +3.3 mV), including the benchmark SM-102/DSPC formulation. These findings indicate that the elevated zeta potential observed in KCl reflect the measurement medium rather than substantially increased surface charge under physiological conditions. Apparent pKa values for all formulations were within the 6.1–6.5 range but showed no correlation with expression profiles, indicating that helper lipid architecture, rather than ionization, drives the observed expression gains (Figure S3a,b). Laurdan assay-based generalized polarization (GP) –pH profiles revealed that higher-performing LNPs exhibited more disordered lipid packing [28] (Figure S3c-e). Nonlinear modeling of the IM dataset revealed an inverse relationship between Laurdan-derived Hill slopes and protein expression (Figure S3e), suggesting that gradual phase-transition kinetics during endosomal maturation may contribute to enhanced translational output. In contrast, the corresponding IV dataset exhibited only a qualitative inverse trend and did not support a robust quantitative correlation (Figure S3f)

From this comprehensive screening, we selected six representative lead HLs spanning the structural design space: two-tailed (PC-06, PEA-DMA-06, PEA-DMA-12) and three-tailed (PEA-DMA-PE-02, CA-DMA-L3-01, PC-PE-03) architectures (Figure 3a). We carried out iterative composition optimization using a Design of Experiments (DOE) approach in JMP on representative helper lipids from each major structural class, namely PEA-DMA-06, PC-06, and CA-DMA-L3-01 (Figure S4). A mixed mixture analysis in JMP showed that the optimal composition (Figure 3b) was determined by two attributes: head group identity (DMA vs. PC) and tail architecture (two-tailed vs. three-tailed). These results established a generalizable, "plug-and-play" framework that could be extended to other helper lipids with similar chemical nomenclature when formulated with Ionizable Lipid A LNPs (Figure S4a–x). Using this framework, we were able to transfer the optimized PEA-DMA-06 composition to other two-tailed, DMA-headgroup helper lipids, such as PEA-DMA-12, as well as PEA-headgroup helper lipids, such as PEA-06. Similarly, the optimized compositions for PC-06 was applicable to both two-tailed and three-tailed PC-based helper lipids, such as PC-PE-03 (Figure S4w). Finally, the optimized composition for CA-DMA-L3-01 carried over to all three-tailed, DMA-based helper lipids, such as PEA-DMA-PE-02. This systematic approach, spanning molecular design through formulation optimization, yielded improved performance across candidates, with side-by-side comparisons of screening and optimized compositions shown in Figure S5, establishing a robust toolkit for tailoring LNP performance across diverse therapeutic and vaccine modalities. The optimized lead compositions as shown in Figure 3b, were used for all subsequent studies. To determine whether helper lipid architecture represents a formulation-specific optimization or a broadly transferable design principle, lead helper lipids were incorporated into clinically relevant ALC-0315- and DLin-MC3-DMA-based LNPs (Figure S6). Despite the substantial differences in chemical structure, ionization behavior, and clinical application of these ionizable lipids, multiple engineered helper lipids consistently enhanced mRNA expression relative to DSPC-containing controls. Importantly, the highest-performing helper lipid architectures identified in the primary screening campaign retained their relative superiority across both vaccine-associated and hepatic delivery platforms. This conservation of performance hierarchy across distinct ionizable lipid systems suggests that helper lipid architecture functions as an orthogonal determinant of LNP efficacy rather than merely a context-dependent formulation component. These results establish helper lipid engineering as a broadly applicable strategy for improving mRNA delivery across clinically relevant LNP platforms. Across both platforms, replacement of conventional DSPC with the novel helper lipids resulted in enhanced mRNA expression, demonstrating that the benefits of helper lipid engineering are not restricted to a single ionizable lipid scaffold. Although the relative performance of individual helper lipids varied between ionizable lipid systems, reflecting context-dependent lipid-lipid interactions, multiple lead structures consistently improved expression in both intramuscular and intravenous delivery settings. These findings establish helper lipid architecture as a transferable and broadly applicable design parameter for mRNA-LNP optimization and suggest that helper lipid selection can be tailored to specific therapeutic modalities and ionizable lipid chemistries. Notably, the formulations evaluated here were not re-optimized for each ionizable lipid system; therefore, additional composition-specific optimization is expected to further enhance performance within individual platforms. Collectively, these data demonstrate the potential of rational helper lipid engineering as a versatile strategy for improving the efficacy of clinically relevant mRNA delivery systems across diverse LNP architectures. Although several 03 Tail formulations exhibited superior IV expression, these gains were not consistently maintained across intramuscular delivery or alternative ionizable lipid platforms. In contrast, the 06 Tail scaffold demonstrated robust activity across multiple administration routes and formulation backgrounds, motivating its selection for further optimization and mechanistic characterization. While several optimized helper lipids achieved higher expression levels, PC-06 emerged as a particularly interesting candidate because it appeared to balance two often competing formulation attributes: delivery potency and storage stability. The PC headgroup was expected to improve mRNA stability, while the Tail-06 architecture preserved delivery activity, resulting in expression levels

15214095, 0, Downloaded from https://advanced.onlinelibrary.wiley.com/doi/10.1002/adma.75746, Wiley Online Library on [17/11/2026]. See the Terms and Conditions (https://onlinelibrary.wiley.com/terms-and-conditions) on Wiley Online Library for rules of use; OA articles are governed by the applicable Creative Commons License

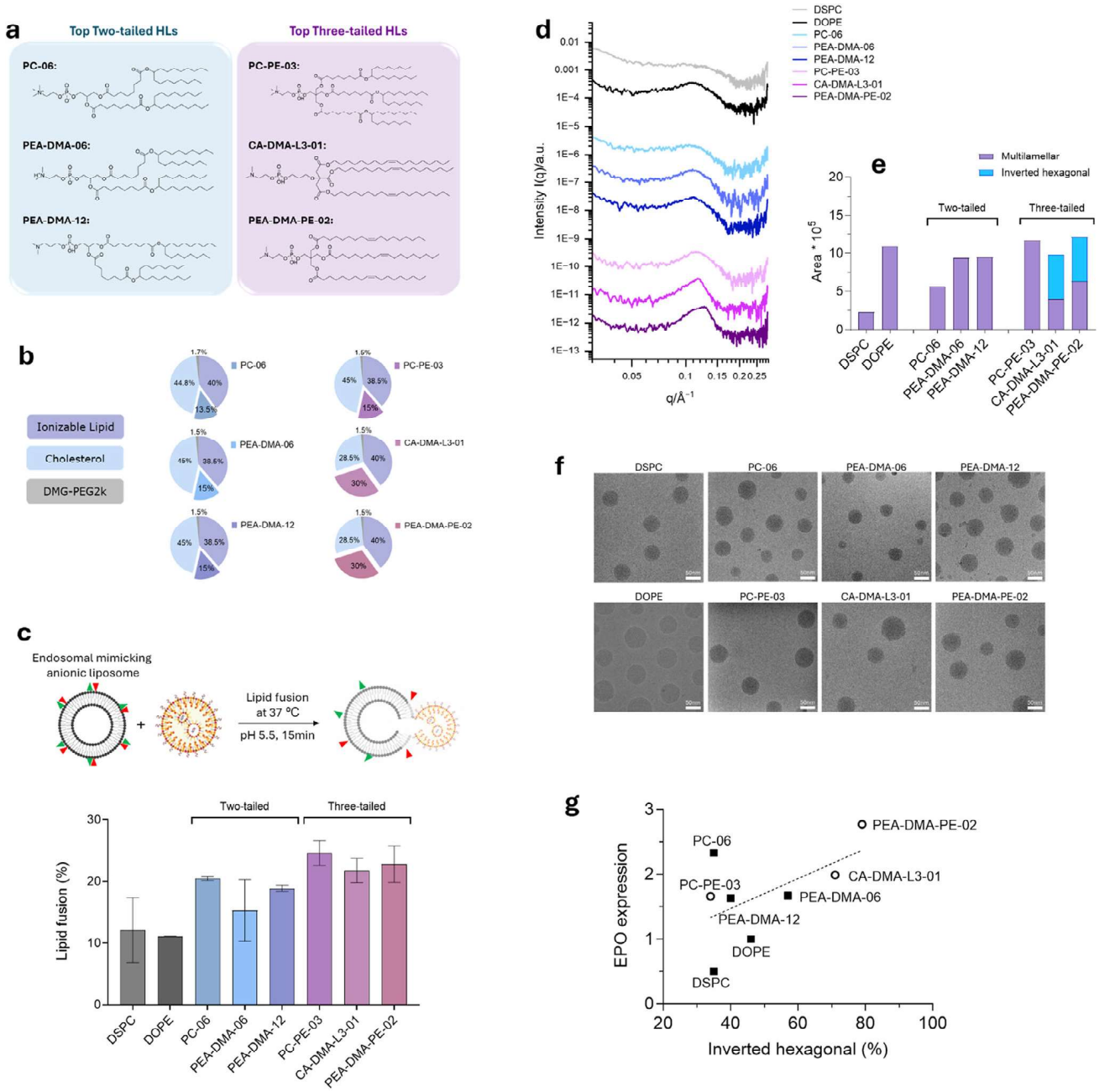


FIGURE 3 | Analytical and biophysical characterization of optimized formulations of top lead two- and three-tailed helper lipids. (a) Comparative structure–activity relationship (SAR) analysis of lead two-tailed (PC-06, PEA-DMA-06, PEA-DMA-12) and three-tailed (PC-PE-03, CA-DMA-L3-01, PEA-DMA-PE-02) helper lipid (HL) structures. (b) Optimized LNP molar compositions derived from JMP-based Design of Experiments (DOE) to maximize translational efficacy for each lead HL scaffold. (c) FRET-based membrane fusion assay evaluating the pH-sensitivity of lead formulations with model endosomal membranes; increased FRET at lower pH indicates enhanced fusogenic potential. Data are presented as mean ± standard deviation (SD) from three independent replicates ($n = 3$) for each helper lipid formulation. Structural characterization via Small-Angle x-ray Scattering (SAXS), including (d) scattering intensity profiles (pH 5.5) and (e) integrated area plots depicting the relative distribution of internal lipid phases (lamellar vs. inverted hexagonal) (f) Representative cryo-electron microscopy (cryo-TEM) images of top-performing HL-LNPs, demonstrating mix of different internal structures (g) Correlation analysis between LNP translational potency and the percentage of inverted hexagonal phase content, identifying internal phase topography as a primary biophysical driver of endosomal escape efficiency. The square and circles represent two- or three-tailed HLs, respectively.

comparable to the highly fusogenic DOPE benchmark without the substantial loss of potency commonly associated with more lamellar phospholipids such as DSPC. Importantly, accelerated stability studies demonstrated improved preservation of mRNA integrity and encapsulation efficiency relative to DOPE (Figure S7). Given the growing importance of thermostable mRNA formulations for vaccine deployment and global distribution, this combination of enhanced stability and maintained delivery performance makes PC-06 a particularly attractive helper lipid scaffold for further development.

15214095, 0, Downloaded from https://advanced.onlinelibrary.wiley.com/doi/10.1002/adma.75746, Wiley Online Library on [17/11/2026]. See the Terms and Conditions (https://onlinelibrary.wiley.com/terms-and-conditions) on Wiley Online Library for rules of use; OA articles are governed by the applicable Creative Commons License

2.2 | Multi-Modal Biophysical Profiling Reveals a Correlation Between Internal Nanostructure and Translational Potency

To elucidate structural and mechanistic determinants of the novel HL library, we integrated multi-modal biophysical characterization spanning molecular membrane fusion to particle morphology. First, the fusogenic potential of LNPs formulated with the top 6 HLs was evaluated using a Förster resonance energy transfer (FRET) membrane-mixing assay under late-endosomal conditions (37°C, pH 5.5). To assess membrane fusion, we monitored NBD-PE dequenching upon LNP fusion with endosome-mimicking vesicles. At physiological pH (7.4), all formulations exhibited comparable lipid-mixing behavior with no significant formulation-dependent differences. However, upon acidification, distinct differences emerged, with the engineered three-tailed helper lipids demonstrating enhanced fusion kinetics relative to the benchmark formulations, consistent with their proposed role in promoting endosomal escape. This assay revealed a strong correlation between enhanced in vivo expression of two- and three-tailed HL derivatives and their superior pH-sensitivity relative to the fusogenic DOPE control (Figure 3c). The architectural design of the hydrophobic tails allowed precise modulation of fusion kinetics, even when the headgroup chemistry remained constant, confirming that tail geometry actively lowers the energetic barrier for endosomal escape [29]. The structural fingerprints of the lead candidates were mapped via orthogonal characterization using cryo-transmission electron microscopy (cryo-TEM) imaging, small-angle x-ray scattering (SAXS) diffraction, and flow field-flow fractionation coupled with multi-angle light scattering (AF4-MALS) [30], enabling a holistic determination of the relationship between lipid packing geometry and macroscopic particle morphology (Figure 3d–g and Figure S8). To resolve the internal organization of these LNPs, we performed SAXS across a pH gradient. In Figure 3d,e, two-tailed HLs exhibited a single Bragg peak ($q \approx 0.11$ Å^{-1}), possibly indicating a uniform ordered phase or the existence of multiple overlapping ordered phases with similar lattice spacing. Conversely, peak deconvolution of the three-tailed HL profiles revealed a bimodal distribution with two distinct peaks separated by approximately 0.015 Å^{-1}. This suggests a coexistence of at least two ordered structural phases, a finding corroborated by cryo-TEM. As shown in Figure S9b, upon acidification to pH 4.5, all formulations underwent dramatic reorganization toward more compact d-spacings ($d = 2\pi/q$). To bridge these nanostructural findings with bulk particle morphology, we employed hierarchical clustering of cryo-TEM micrographs (Figure S9d), alongside AF4-MALS. DOPE formulations formed a distinct structural class characterized by hexagonal phases and blebs, whereas DSPC and PC-06 clustered as rigid lamellar bilayers. The potent leads identified in this study, PEA-DMA-PE-02 and PC-PE-03, exhibited a multifaceted lamellar baseline characterized by varying degrees of angularity and hexagonal domains. This nonspherical, polyhedral morphology aligns with established structural paradigms in which faceted LNP surfaces significantly enhance endosomal escape and cytosolic mRNA delivery [31, 32]. MALS-derived shape factors ($\rho = Rg/Rh$) provided a quantitative descriptor for these geometries (Figure S8b). While standard two-tailed LNPs resembled uniform hard spheres ($\rho \approx 0.77$), PEA-DMA-PE-02 exhibited a higher factor ($\rho = 0.88$), corresponding to the unique "polygonal" or faceted morphologies observed via cryo-TEM. Conversely, CA-DMA-L3-01 and PC-PE-03 approached shape factors of 1.0. Analysis of the chromatographic "shoulders" in these populations suggests a heterogeneous cargo distribution, where mRNA may be preferentially partitioned into larger, more ordered sub-populations, while the primary population adopts a hollow, multi-lamellar architecture. Peak deconvolution of SAXS chromatograms revealed a significant correlation between high-potency formulations and the emergence of a strong peak, probably an inverse hexagonal (H_{II}) like ordering at low pH. We propose that the steric bulk of the three-tailed architecture facilitates this transition by favoring negative interfacial curvature. While the SAXS profiles do not allow unequivocal discrimination among all possible nonlamellar mesophases, the combined SAXS, cryoTEM, FRET, and MDs analysis consistently indicate increased inverse-curvature organization in the three-tailed helper lipid formulations. Crucially, the relative abundance of the second peak at pH 4.5 directly mapped to hEPO expression levels, identifying this fusogenic phase as a primary determinant of cytosolic mRNA release (Figure 3g). These data collectively demonstrate that structural innovation in the helper lipid tail, specifically the transition to three-tailed scaffolds, promotes a highly ordered internal environment. However, SAXS alone cannot determine what exact internal structures are present, especially for a heterogenous modality such as LNPs. Therefore, future improvements to methodology to decrease heterogeneity along with additional orthogonal techniques should be employed to provide a more coherent analysis. Through this structural polymorphism, the LNP remains stable at physiological pH but rapidly adopts fusogenic architectures upon endosomal acidification.

2.3 | Optimized Helper Lipids Enable Improvement in Hepatic mRNA Delivery With Maintained Safety Profile

Building on our hEPO screening, we interrogated the extent to which novel HL scaffolds could refine the biodistribution and therapeutic potency of mRNA-LNPs. Intravenously administered mRNA-LNPs exhibit an inherent tropism for the liver, a process governed by the spontaneous adsorption of endogenous Apolipoprotein E (ApoE) and subsequent LDLR-mediated endocytosis [33]. While multiple avenues have been investigated to refine this tropism, such as active targeting via GalNAc-ligands [34] or tailored passive targeting through lipid component optimization (SORT-LNP strategy) [35], achieving high-efficiency hepatic partitioning while minimizing extrahepatic sequestration, particularly in the spleen, remains critical for expanding the therapeutic index [36]. With optimized composition and using a firefly luciferase (FFLuc) reporter (Figure 4a), we observed that the two-tailed PEA-DMA-12 and PEA-DMA-06 HLs provided modest 1.8- and 2.7-fold enhancements in liver expression over the DOPE benchmark, while the three-tailed tri-alkyl architectures demonstrated markedly superior performance, with PC-PE-03, CA-DMA-L3-01, and PEA-DMA-PE-02 exhibiting robust bioluminescent signals and outperforming the DOPE reference by 5.5-, 7.5-, and 19.5-fold, respectively (Figure 4b,c). These findings reveal a strong correlation between an increased number of unsaturated alkyl-chains and enhanced hepatic expression.

15214095, 0, Downloaded from https://advanced.onlinelibrary.wiley.com/doi/10.1002/adma.75746, Wiley Online Library on [17/11/2026]. See the Terms and Conditions (https://onlinelibrary.wiley.com/terms-and-conditions) on Wiley Online Library for rules of use; OA articles are governed by the applicable Creative Commons License

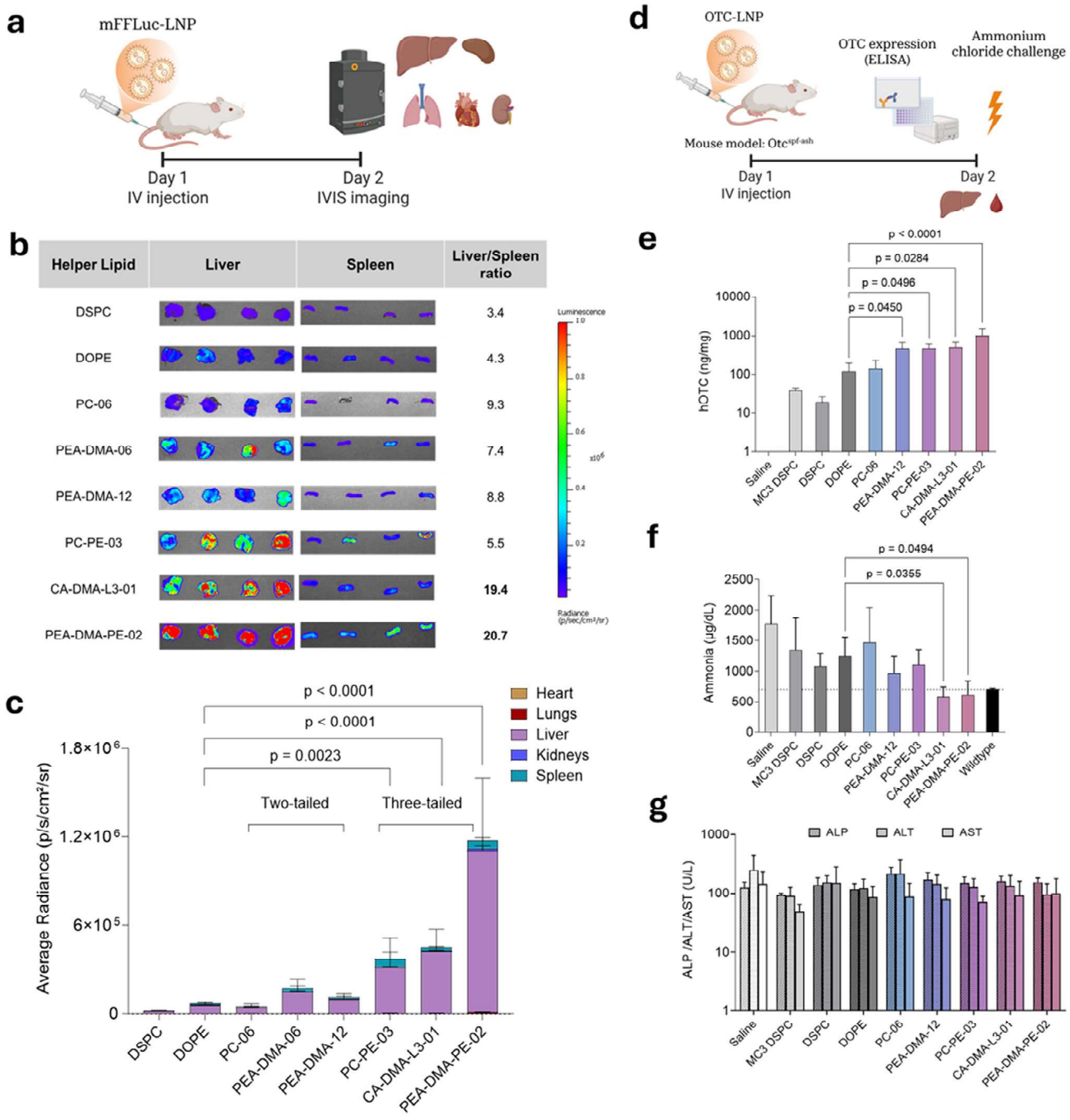


FIGURE 4 | Biodistribution with FFluc mRNA-LNPs and therapeutic efficacy for hepatic protein replacement in a mouse model of Ornithine Transcarbamylase (OTC) deficiency for the lead helper lipids. Systemic biodistribution and expression kinetics of optimized helper lipid (HL) formulations. (a) Experimental timeline for intravenous (IV) administration of LNPs encapsulating firefly luciferase (mFFLuc) mRNA.(b) Representative *ex vivo* IVIS bioluminescence images of livers and spleen 24-hours post-injection, demonstrating significantly enhanced hepatic protein expression for three-tailed leads CA-DMA-L3-01 and PEA-DMA-PE-02 compared to DSPC and DOPE benchmarks. c) Quantitative analysis of liver-to-spleen radiance ratios and percentage of total hepatic signal, highlighting the superior liver expression of three-tailed helper lipids. Male BALB/c mice (6-8 weeks old) were injected with LNPs loaded with FFLuc mRNA at a dose of 0.017 mg/kg via intravenous route. All data are presented as the mean ± SD (n = 4).Therapeutic evaluation in the OTC $^{spf\text{-}ash}$ mouse model. (d) Study design for human OTC (hOTC) mRNA delivery (dose 0.5 mg/kg) followed by an ammonium chloride challenge to assess functional rescue. (e) Quantification of hOTC protein levels in liver homogenates, where the hierarchy of expression mirrors the biodistribution profiles observed in (c). (f) Serum ammonia levels following challenge; top-performing HL-LNPs provided robust protection against hyperammonemia, correlating with increased hepatic hOTC expression. (g) Safety and tolerability assessment 24-hour post-treatment. Serum biomarkers for liver function, including alanine aminotransferase (ALT), aspartate aminotransferase (AST), and alkaline phosphatase (ALP), remain within normal limits, confirming the favorable safety profile of the novel helper lipid designs. OTC$^{spf\text{-}ash}$ males (4-8 weeks, Jackson Laboratories) were dosed with LNPs encapsulating hOTC mRNA. All data are presented as a mean ± SD (n = 5). Statistical significance was determined by one-way ANOVA followed by Dunnett's multiple comparison test against DOPE control.

15214095, 0, Downloaded from https://advanced.onlinelibrary.wiley.com/doi/10.1002/adma.75746, Wiley Online Library on [17/11/2026]. See the Terms and Conditions (https://onlinelibrary.wiley.com/terms-and-conditions) on Wiley Online Library for rules of use; OA articles are governed by the applicable Creative Commons License

The tri-alkyl formulations achieved a liver-to-spleen distribution ratio of approximately 20:1, representing a 5-fold improvement over the 4:1 ratio observed for standard DSPC- and DOPE-based compositions (Figure 4b). To elucidate the mechanism underlying this selectivity, we characterized ApoE association kinetics via quartz crystal microbalance with dissipation (QCM-D). While DOPE showed greater protein adsorption than DSPC, we found no significant difference in ApoE binding among the most potent two- and three-tailed variants (Figure S10). These data suggest that the superior hepatic delivery and organ-selectivity observed with these novel architectures are independent of differential ApoE binding. Instead, their enhanced therapeutic index is likely governed by optimized pH-responsive behavior and enhanced membrane fusion and endosomal escape-associated activity facilitated by unique tail geometries. We then validated the therapeutic utility of our optimized scaffolds in the *spf-ash* mouse model of Ornithine Transcarbamylase Deficiency (OTCD), a severe urea cycle disorder characterized by toxic hyperammonemia. We benchmarked our lead three-tailed candidate, PEA-DMA-PE-02, against the standard controls DSPC and DOPE (all three LNPs formulated with ionizable lipid A), as well as the foundational MC3 DSPC-LNP platform, a clinically validated ionizable lipid system. PEA-DMA-PE-02 achieved robust hepatic hOTC expression of ~1,000 ng/mg total liver protein, representing an approximately 27-fold enhancement over MC3 LNPs and an 8-fold increase relative to DOPE-based LNPs. (Figure 4e). This supraphysiological enzyme production was translated directly into functional metabolic rescue. Following a systemic ammonia challenge, saline-treated *spf-ash* mice showed elevated serum ammonia levels (1,700 µg/dL). In contrast, treatment with PEA-DMA-PE-02 or CA-DMA-L3-01 effectively normalized ammonia concentrations to wild-type levels (800 µg/dL) (Figure 4f). Similarly, the two-tailed PEA-DMA-12 showed a significant 4-fold increase in hOTC expression and a concomitant reduction in ammonia levels. Importantly, this enhanced potency was achieved without elevating serum biomarkers of hepatic distress (ALT, AST, and ALP), suggesting an improved therapeutic index without overt toxicity (Figure 4g). Notably, the observed efficacy gains were achieved solely through modification of the helper lipid component, while maintaining the same ionizable lipid framework, underscoring the capacity of helper lipid engineering to substantially improve therapeutic output without redesigning the core delivery platform. Collectively, these results demonstrate that structural innovation in helper lipid tails, specifically the transition to tri-alkyl scaffolds, can resolve the delivery bottlenecks inherent to systemic metabolic therapy, providing a robust, well-tolerated platform for hepatic protein replacement.

2.4 | Helper Lipid Engineering Amplifies Antigen Expression to Drive Superior Vaccine Immunogenicity

To assess the suitability of the novel HL scaffolds for vaccine applications, we first tested LNPs with compositions as in Figure 3b, for their ability to transfect antigen presenting cells (APCs), a prerequisite for robust adaptive responses. Using primary human dendritic cells (hDCs), we quantified the relationship between LNPs uptake and protein output via a dual-modality readout: single molecule- fluorescence in situ hybridization (smFISH) for intracellular mRNA and immunofluorescence (IF) for encoded protein (Figure 5a). These analyses revealed a pronounced decoupling between cellular internalization and protein translation that is defined by HL chemistry. DOPE-containing LNPs showed the highest cellular uptake but yielded poor protein expression. In contrast, LNPs with PEA-DMA-PE-02 and PC-PE-03 achieved the highest protein expression despite only intermediate cellular uptake, suggesting that translation efficiency and endosomal escape, rather than cellular entry, represent the dominant rate-limiting steps in hDC-dependent HL delivery. We next asked whether the in vitro translational advantages conferred by specific HLs translate into superior functional immunity in vivo. BALB/c mice received a 2-dose intramuscular regimen (0.4 µg) of mRNA LNPs- encoding influenza A/Tasmania/503/2020 (H3N2) hemagglutinin (HA). Hemagglutination inhibition (HAI) assays established a clear potency hierarchy (Figure 5b): PEA-DMA-12 ($p = 0.0004$) and PEA-DMA-PE-02 ($p = 0.008$) significantly exceeded the DOPE control, whereas DSPC reduced titers relative to DOPE ($p = 0.021$). Clinical benchmarks ALC-0315 and SM-102, both formulated with DSPC helper lipid, yielded titers comparable to the DOPE control formulation.

Within a common Ionizable Lipid A background, helper lipid engineering substantially enhanced vaccine performance, with several formulations generating immune responses comparable to or exceeding those observed with clinically validated ALC-0315- and SM-102-based LNP benchmarks.

These data corroborate the hDC findings, demonstrating that HL-driven gains in protein expression are mirrored by superior functional antibody responses in vivo (Figure 5c). To bridge species differences and evaluate clinical translatability, we employed the fully human MIMIC system, which recapitulates salient features of lymphoid and peripheral tissue microenvironments (Figure 5d). Within the MIMIC Lymphatic Tissue Equivalent (LTE)—a 3D co-culture of primary human B cells, T cells, and APCs that support germinal center-like interactions and antigen specific-IgG production—we quantified antibody responses to HA mRNA formulated across HL variants. CA-DMA-L3-01 elicited the highest anti-HA titers, outperforming DOPE, while PEA-DMA-12, PEA-DMA-PE-02, and PC-PE-03 matched or trended higher than the DOPE benchmark (Figure 5e). Notably, the rank order of immunogenicity in the human LTE system aligned with murine HAI outcomes, with PEA-DMA-12 and PEA-DMA-PE-02 consistently among the top performers across both platforms. This cross-species concordance strengthens confidence in the translational potential of the lead HL scaffolds and provides critical preclinical derisking for clinical advancement.

Because HL chemistry can modulate LNP surface properties and thereby influence cellular biodistribution, we profiled innate cell targeting in the MIMIC Peripheral Tissue Equivalent (PTE), a 3D collagen matrix containing primary human monocytes, macrophages, and other immune cells that emulates the injection-site milieu. Flow cytometry revealed that classical monocytes ($CD14^+CD16^-$) were the predominant transfected population across all formulations (Figure 5f,g), consistent with their role as first responders and initiators of downstream adaptive responses. While overall tropism remained conserved, indicating that HL modifications do not reroute targeting, transfection efficiency within monocytes was highly sensitive to HL architecture. Three-tailed variants substantially increased

15214095, 0, Downloaded from https://advanced.onlinelibrary.wiley.com/doi/10.1002/adma.75746, Wiley Online Library on [17/11/2026]. See the Terms and Conditions (https://onlinelibrary.wiley.com/terms-and-conditions) on Wiley Online Library for rules of use; OA articles are governed by the applicable Creative Commons License

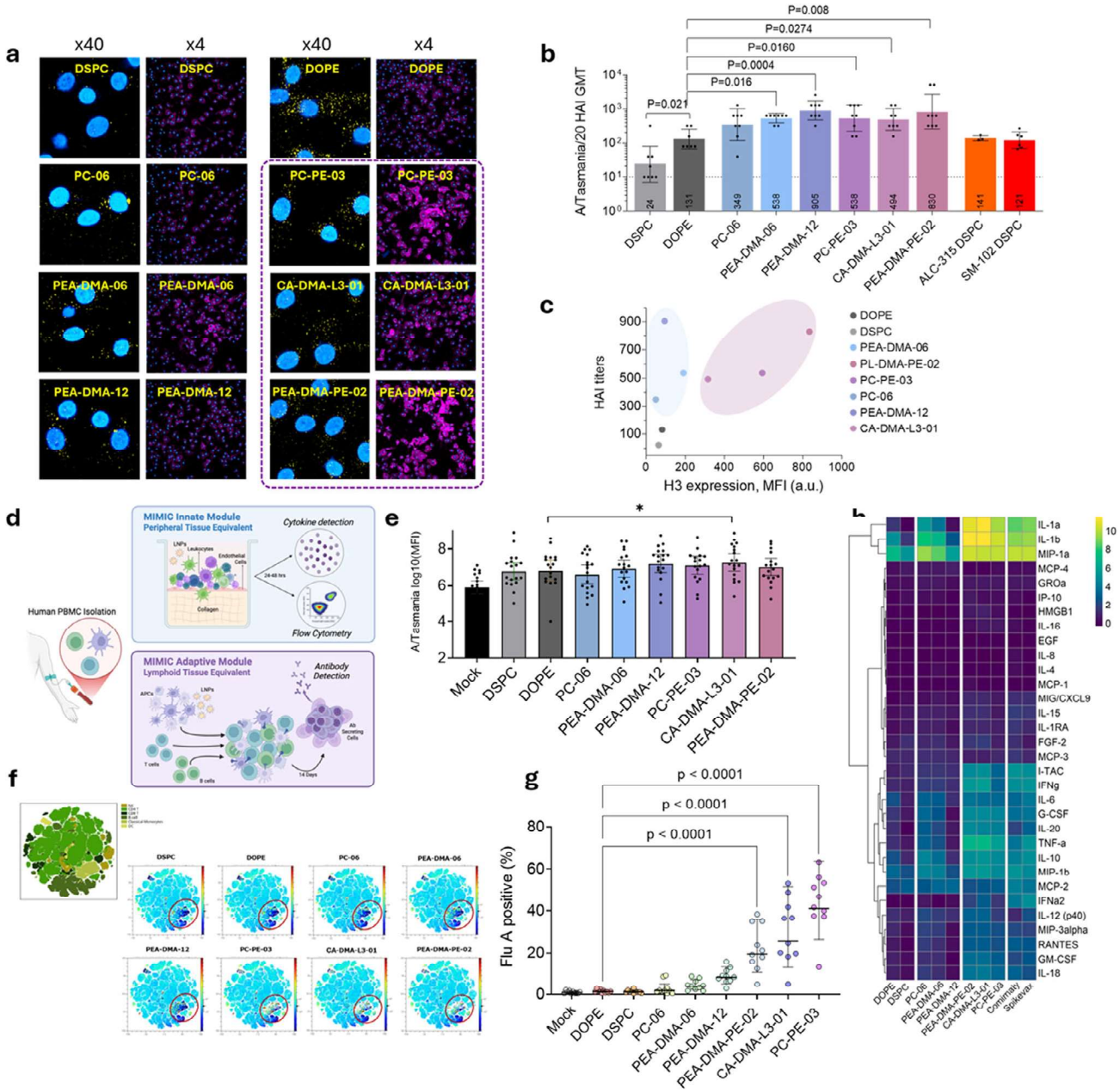


FIGURE 5 | Top Helper Lipid Formulations Enhance Antigen Expression and Modulate Immunogenicity and Reactogenicity (a) smFISH and immunofluorescence (IF) imaging for quantifying mRNA uptake and protein expression, respectively in human dendritic cells (hDCs). smFISH or IF was performed on fixed hDCs transfected with a dose of 1 μg/million cells. Representative smFISH and IF images of hDCs showing mRNA (Stellaris Quasar 670 probe set, yellow) uptake and protein expression (AF647-labeled Anti-H3 mAb, magenta), respectively. Nuclei (DAPI) are shown in blue. Representative smFISH images shown are cropped from 63x maximum intensity projection (MIP) images to highlight the mRNA spots. The representative IF images shown are 20x MIP images. (b) BALB/c mice (n = 8 per group) were immunized twice intramuscularly (IM), 3 weeks apart with 0.4 μg of LNPs with different helper lipids encapsulating Tasmania HA mRNA. Serum titers were measured by hemagglutinin inhibition assay (HAI) against homologous A/Tasmania/503/2020 H3N2 Influenza virus strain and GMT (geometric mean titers) were graphed for DOPE, DSPC, PC-06, PEA-DMA-06, PEA-DMA-12, PC-PE-03, CA-DMA-L3-01, PEA-DMA-PE-02, ALC-0315 DSPC (GMT of n = 2 studies) and SM-102 DSPC (GMT of n = 6 studies). Ordinary one-way ANOVA with Dunett's test was performed to show statistical significance between groups. (c) Plot showing correlation between the mean in vitro protein (H3) expression in hDCs ($n = 3$ technical replicates) and mean in vivo HAI titers ($n = 8$ mice). (d) Overview of the MIMIC innate (PTE) and adaptive (LTE) modules: PTE enables rapid characterization of cytokine and innate cellular responses to LNP-delivered mRNA, while LTE models lymphoid microenvironments to measure downstream T-cell activation, B-cell differentiation, and antibody secretion. (e) Antibody responses measured in the MIMIC LTE system. Bar graph showing $\log_{10}$-transformed mean fluorescence intensity (MFI) of influenza A/Tasmania–specific antibody responses following treatment with each mRNA–LNP formulation in the LTE module. Each point represents an individual donor; bars indicate geometric mean ± geometric standard deviation. N = 18 donors. (f) Multiparametric flow cytometry analysis of Flu HA expression in the MIMIC PTE system. Opt-SNE maps generated from CD3, CD4, CD8, CD19, CD56, CD14, CD16, CD11c, and HLA-DR expression in hPBMCs treated

15214095, 0, Downloaded from https://advanced.onlinelibrary.wiley.com/doi/10.1002/adma.75746, Wiley Online Library on [17/11/2026]. See the Terms and Conditions (https://onlinelibrary.wiley.com/terms-and-conditions) on Wiley Online Library for rules of use; OA articles are governed by the applicable Creative Commons License

monocyte transfection: CA-DMA-L3-01 reached 30.4%, PEA-DMA-PE-02 22.4%, and PC-PE-03 43.9%, compared with 8.9% for the two-tailed PEA-DMA-12 and near-baseline DOPE (Figure 5g). Thus, HL design can markedly boost antigen expression in intended target cells without altering desired cellular specificity.

To characterize innate activation and anticipate reactogenicity, we measured cytokines in PTE supernatants 24 h post-exposure (Figure 5h and Figure S11). HL composition exerted a strong and differentiable influence on the innate signature. Among the two-tailed lipids, PEA-DMA-12 reduced IL-1β relative to DOPE, suggesting a tempered inflammatory profile, whereas PC-06 and PEA-DMA-06 increased IL-1β. Three-tailed architectures (PEA-DMA-PE-02, CA-DMA-L3-01, PC-PE-03) induced higher overall cytokines, including IL-1β and IFN-γ. Three-tailed helper lipids elicited higher cytokine responses than two-tailed architectures. Although not directly investigated herein, this effect may be linked to the enhanced membrane fusion, endosomal escape, and delivery potency observed for three-tailed lipids. Recent studies have demonstrated that productive LNP-mediated endosomal escape can activate endosomal damage-sensing pathways that contribute to inflammatory cytokine production [37], raising the possibility that the increased cytokine responses observed with the three-tailed helper lipids are associated with their enhanced intracellular delivery efficiency. Crucially, when benchmarked against the clinically approved mRNA vaccines Comirnaty (BNT162b2) and Spikevax (mRNA1273), tested under identical conditions, cytokine magnitudes for the three-tailed leads remained within a similar range. Given the extensive real world safety experience for these vaccines, the observed in vitro innate profiles align with the clinical viability of the most potent HL candidates.

Together, these multi-platform results provide a design framework for tailoring LNP vaccines by HL selection. The two-tailed PEA-DMA-12 emerged as an optimized scaffold that couples enhanced potency with a muted pro-inflammatory signature. For applications requiring maximal stimulation, three-tailed architectures provide a further step-change: CA-DMA-L3-01 shows superior antibody induction in human LTE and higher monocyte transfection, with innate responses that remain within clinically validated safety windows. Such profiles are well suited to scenarios demanding rapid and durable immunity, including pandemic preparedness, immunosenescent populations, or single dose regimens. The concordance between murine HAI and human MIMIC responses validates the translational relevance of lead HLs and derisks clinical progression. More broadly, HL engineering emerges as a powerful lever to tune the immunogenicity–reactogenicity balance while preserving targeting, enabling population- and indication-specific optimization anchored to established clinical benchmarks.

2.5 | Biophysical Drivers of LNP Potency: Energetic Landscapes and Internal Organization

To elucidate the biophysical mechanisms governing LNP potency, we performed coarse-grained Martini MDs simulations to map the energetic landscapes of membrane fusion. By isolating the energetic contributions of the helper lipid architecture while maintaining identical ionizable lipid, cholesterol, and PEG components, we characterized the thermodynamic stability of the stalk intermediate (ΔG-stalk) and the activation energy required for membrane fusion initiation (ΔG-barrier) [38, 39]. Across lead HLs, ΔG-stalk ranged from -24.94 to -75.98 kJ/mol, while ΔG-barrier varied between 8.08 and 25.25 kJ/mol (Figure 6a,b). These simulations revealed five key design principles: higher tail number (3 vs 2), unbranched architectures, tail unsaturation, tertiary amine headgroups, and optimized linker topography. A prominent "tail number effect" emerged, with three-tailed scaffolds consistently outperforming two-tailed analogs. Specifically, PEA-DMA-PE-02 (ΔG-stalk = -75.98 kJ/mol) and CA-DMA-L3-01 (ΔG-stalk = -59.58 kJ/mol) demonstrated stalk formation energies up to 99% more favorable than DOPE, likely by facilitating the negative spontaneous curvature required for fusion.

Isolating the effect of tail branching revealed that unbranched architectures are energetically privileged, providing a 24%–58% thermodynamic advantage over branched counterparts such as PC-PE-03 in three-tailed systems. This suggests that, as tail cardinality increases, branching introduces steric hindrance and packing constraints that penalize the tight curvature of the fusion stalk. Unsaturation acted as an additional driver of fusion kinetics.

The combination of three-tailed lipids and unsaturation in unbranched scaffolds achieved the most favorable energetics by synergistically enhancing membrane fluidity. Notably, these computational predictions were independently supported by experimental FRET-based membrane-mixing assays, which demonstrated enhanced pH-dependent membrane fusion and accelerated fusion kinetics for the same formulations.

Furthermore, headgroup chemistry dictated the magnitude of membrane destabilization; tertiary amine headgroups (e.g., PEA-DMA-06) provided a 41% thermodynamic advantage and a ~60% reduction in ΔG-barrier compared with quaternary ammonium analogs (PC-06). The topography of the headgroup-linker region proved equally critical, as extending the pre-phosphate linker from one to two carbons (PEA-DMA-12) improved ΔG-stalk by 43% and reduced the activation barrier by half.

Figure 6c,d show self-assembly simulations corroborating these energetic findings and reveal that formulations with the most

for 24 h with mRNA-LNPs or cell culture media (Mock). Colored clusters highlight cell populations showing differential Flu HA$^+$ hPBMC abundance, identified using FlowSOM and analyzed within immune subsets. (g) Percentage of Flu HA$^+$ cells within the classical monocyte subset (CD14$^+$CD16$^-$), shown as scatter plots with geometric mean ± geometric standard deviation. Opt-SNE projections were automatically generated using OMIQ software. (h) Cytokine secretion in response to mRNA-LNPs in the MIMIC PTE system. The MIMIC PTE system was generated using donor PBMCs and treated with each HL mRNA–LNP formulation. After 24 h, culture supernatants were collected and cytokine levels were quantified by Luminex. Fold-change relative to media-only controls (Mock) was calculated, and the heatmap shows hierarchical clustering of Log_2 fold-change cytokine responses. N = 10 donors.

15214095, 0, Downloaded from https://advanced.onlinelibrary.wiley.com/doi/10.1002/adma.75746, Wiley Online Library on [17/11/2026]. See the Terms and Conditions (https://onlinelibrary.wiley.com/terms-and-conditions) on Wiley Online Library for rules of use; OA articles are governed by the applicable Creative Commons License

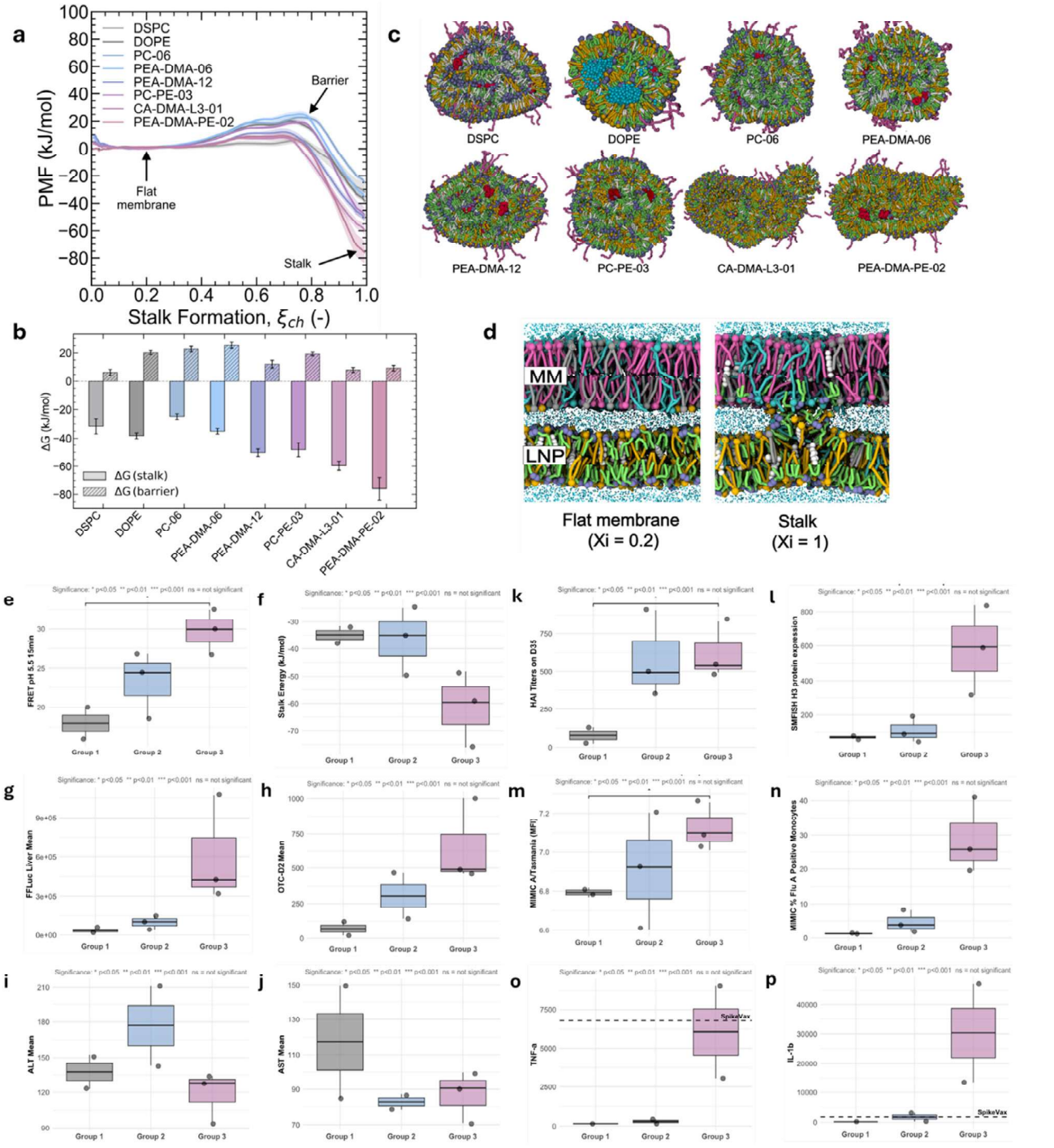


FIGURE 6 | Membrane Fusion and Coarse-Grained Simulations of LNP Self-Assembly for novel HL leads. (a) Potential of mean force (PMF) profiles of stalk formation for varying helper lipids, with error bars displayed as shaded regions. (b) Free energy of stalk formation (ΔGstalk) and barrier (ΔGbarrier), obtained from the PMF profiles shown in panel a. Error bars represent one standard error (SE), estimated by bootstrapping. In panels A and B, helper lipids are shown as yellow sticks with phosphate groups represented as yellow spheres; ionizable lipid is shown as green sticks with the headgroup represented as blue spheres; cholesterol is shown as grey sticks; PEG-lipid is shown in pink. (c) Final snapshots from MARTINI coarse-grained self-assembly simulations showing helper lipid-dependent LNP internal structures: multilamellar (DSPC, PC-06, PEA-DMA-06), inverted micellar (PC-PE-03, CA-DMA-L3-01, PEA-DMA-PE-02), mixed (PEA-DMA-12), and inverted micellar core with water pockets (DOPE). The poly(A) tail is shown in red. Water molecules and ions are omitted for clarity, except for DOPE, where water molecules inside the LNP core are shown. (d) Representative structures from membrane fusion simulations at two key stages: at Xi = 0.2, depicting a flat membrane configuration where the two membranes are separated by 18 water beads per nm^2, and at Xi = 1, depicting the formed stalk structure. The upper membrane represents the model membrane, and the lower membrane represents the LNP. (e-p) t-test analysis comparing the performance between DOPE and DSPC control (Group 1, gray), 2-tail HL (Group 2, blue), and 3-tail HL (Group 3, mauve) for respective attributes evaluated and listed on the y-axis. $*p < 0.05$ represents statistical significance between groups.

15214095, 0, Downloaded from https://advanced.onlinelibrary.wiley.com/doi/10.1002/adma.75746, Wiley Online Library on [17/11/2026]. See the Terms and Conditions (https://onlinelibrary.wiley.com/terms-and-conditions) on Wiley Online Library for rules of use; OA articles are governed by the applicable Creative Commons License

favorable energetics predominantly formed extensive inverted micelle networks. In contrast, poorer performers like DSPC formed predominantly multilamellar structures, which limit the curvature flexibility required for efficient fusion. While 20 nm LNP simulations showed discrete inverted micelles, experimental SAXS data revealed H_{II} hexagonal phases. This discrepancy can be reconciled through a size-dependent structural evolution model, in which inverted micelles serve as transient nucleation sites that coalesce into extended cylindrical hexagonal channels as particle volume increases (coarse grain self-assembly simulations movies in Movies S1). To investigate how composition influences stalk energetics (ΔG-stalk), mass density distributions were analyzed (Figure S12). While overall morphology remained consistent, individual lipids species exhibited distinct localization patterns: ionizable lipids consistently enriched the stalk, whereas helper lipids varied; DOPE localized within the core, while others accumulated peripherally. Three-tailed lipids generally showed higher densities than two-tailed variants. Conversely, DOPC and DOPS were consistently depleted from the core, and cholesterol enrichment patterns varied depending on the specific helper lipid formulation. Collectively, these simulations define a mechanistic framework linking helper lipid architecture to membrane fusion energetics, quantitatively explaining the enhanced functional performance of LNPs with the lead novel helper lipids. These computational profiles correlated strongly with our experimental hEPO expression data and in vivo therapeutic and vaccine models. By fundamentally lowering the energetic barrier for endosomal escape, by up to 64%, these optimized helper lipid architectures resolve the disconnect between molecular design and macroscopic delivery efficacy. This establishes a direct predictive relationship between helper lipid molecular architecture, stalk formation energetics, and therapeutic output, providing a robust biophysical roadmap for next-generation mRNA therapeutics.

Collective analysis further revealed that helper lipid tail number correlates with enhanced late-endosomal (pH 5.5) sensitivity and stalk formation (Figure 6e,f), with three-tailed formulations showing additive benefits over two-tailed HLs (Group 2) and control formulations (Group 1). These mechanistic improvements translated to superior protein expression following IV (FFLuc, hOTC; Figure 6h,e) and IM (H3 in hDC and monocytes; Figure 6l–n) administration. However, in vivo H3 inhibitory HAI titers (Figure 6k) did not correlate with tail number, with PEA-DMA-12 (a two-tailed HL) generating the highest titers. While three-tailed formulations reduced ALT/AST levels despite increased liver protein expression (Figure 6i,j) following IV administration, they also induced higher levels of reactogenic cytokines, including IL-1β and TNF-α, substantially exceeding control group 1 (Figure 6o,p). In contrast, PEA-DMA-12 (two-tailed HL) exhibited the lowest reactogenicity profile. Statistical analysis (t-test) indicates three-tailed helper lipids are optimal for IV therapeutic delivery, while two-tailed formulations are preferable for IM vaccine applications.

Together, these findings reposition the helper lipid from a passive stabilizing excipient to an actively programmable regulator of LNP stability, membrane energetics, endosomal escape, and downstream potency. Notably, helper lipid performance differed between intravenous and intramuscular administration. Formulations that excelled in hepatic delivery were not always the most effective in vaccine applications, likely reflecting the distinct biological barriers and immunological requirements associated with each route. While three-tailed helper lipids generally produced the strongest IV delivery, several two-tailed architectures generated robust vaccine responses with a more moderate cytokine profile, suggesting that optimal helper lipid design may be application- and route-dependent. By identifying tail number and architecture, linker topology, and headgroup chemistry as dominant and predictive design variables, this work establishes helper lipid architecture as a previously underappreciated but decisive lever for engineering next generation mRNA delivery systems beyond the limits of ionizable lipid optimization. Beyond improving delivery potency, the ability of helper lipid architecture to influence nanoparticle physicochemical properties and biological interactions suggests potential opportunities to modulate tissue tropism. Investigation of helper lipid-directed extrahepatic delivery represents an important future direction arising from this work. The ability of engineered helper lipids to improve both vaccine-relevant and therapeutic mRNA-LNP systems suggests that helper lipid architecture represents a modality-agnostic engineering lever for next-generation nucleic acid delivery.

3 | Conclusion

This work establishes helper lipid architecture as a previously underappreciated but highly programmable determinant of mRNA-LNP performance. By identifying transferable structure-function relationships that connect helper lipid composition to membrane fusion energetics, internal nanoparticle organization, and biological activity, we demonstrate that helper lipid engineering can serve as an orthogonal optimization strategy alongside ionizable lipid design. Our systematic exploration of over 80 rationally designed scaffolds reveals that headgroup chemistry, linker topology, and tail cardinality directly govern the energetic landscape of membrane fusion and endosomal escape. The mechanistic insights from MDs simulations—particularly the correlation between inverse hexagonal like ordering abundance and translational potency—establish a quantitative link between lipid geometry and functional delivery. This structure-function relationship proved robust across distinct ionizable lipid platforms (ALC-0315, DLin-MC3-DMA), indicating that helper lipid optimization is a generalizable design lever independent of the ionizable lipid scaffold.

Across therapeutic and vaccine applications, and across multiple clinically relevant ionizable lipid platforms, helper lipid optimization reshaped nanoparticle structure, membrane fusion energetics, and biological performance. The two-tailed/three-tailed dichotomy revealed a nuanced trade-off: three-tailed architectures (PEA-DMA-PE-02, CA-DMA-L3-01) maximize potency for intravenous route of administration for hepatic delivery, while two-tailed variants (PEA-DMA-12) achieve superior balance between immunogenicity and tolerability for intramuscular vaccine applications. This modularity suggests that helper lipid selection can be tailored to specific therapeutic objectives rather than treated as a fixed component.

Going forward, these design principles open several avenues for next-generation LNP optimization. First, the quantitative SAR framework enables rational screening of additional chemical

15214095, 0, Downloaded from https://advanced.onlinelibrary.wiley.com/doi/10.1002/adma.75746, Wiley Online Library on [17/11/2026]. See the Terms and Conditions (https://onlinelibrary.wiley.com/terms-and-conditions) on Wiley Online Library for rules of use; OA articles are governed by the applicable Creative Commons License

space; particularly exploring linker and headgroup. Second, the demonstrated transferability across ionizable lipids suggests that helper lipid engineering could accelerate development of LNPs for emerging modalities. Third, the human MIMIC platform validation provides a bridge to clinical translation, reducing the species-translation gap that has historically limited preclinical LNP predictions. Finally, the mechanistic understanding of pH-dependent phase transitions may inform rational design of next generation LNPs. By defining transferable molecular design principles that connect lipid architecture to functional delivery outcomes, this work provides a broadly applicable framework for the rational engineering of next-generation mRNA medicines.

4 | Experimental Section

4.1 | Materials

1,2-dimyristoyl-rac-glycero-3-methoxypolyethylene glycol (DMG-PEG), 1,2-dioleoyl-sn-glycero-3-phosphoethanolamine (DOPE), and 1,2-distearoyl-sn-glycero-3-phosphocholine (DSPC) were obtained from Avanti Polar Lipids (Alabaster, AL). Cholesterol was purchased from Sigma-Aldrich. All other chemicals and reagents were commercially available and used without further purification. Ionizable lipid A and the novel helper lipids were synthesized internally and provided by Sanofi. mRNA constructs, namely human erythropoietin (hEPO), firefly luciferase (FFluc), and hemagglutinin (HA) from A/California/04/2009, were synthesized by in vitro transcription using RNA polymerase to transcribe mRNA from a plasmid DNA template encoding the desired genes. The resulting purified precursor mRNA was further modified via enzymatic addition of a 5′ cap structure (Cap 1) and an approximate 200-nucleotide 3′ poly(A) tail.

4.2 | Preparation of LNPs

The mRNA-encapsulating LNP formulations were prepared as described earlier [28].

LNPs were prepared by rapid mixing of an ethanolic lipid phase with an aqueous mRNA phase using a T-mixer configuration as previously described. The aqueous phase consisted of mRNA diluted to 0.0833 mg mL^{-1} in pH 4.5 citrate buffer (1 mM sodium citrate, 150 mM NaCl). The organic phase contained the ionizable lipid, helper lipid, cholesterol, and PEG-lipid dissolved in ethanol at the desired molar ratios. The aqueous and organic phases were mixed at a 4:1 flow-rate ratio (aqueous: organic) using gear pumps connected to a 1/16′ nylon T-mixer at a total flow rate of 250 mL/minute. Formulations were prepared at fixed N/P ratios as indicated for each formulation. Following particle formation, LNPs were dialyzed and subjected to ultrafiltration/diafiltration into the final formulation buffer, sterile filtered, adjusted to the target concentration, and stored at -80°C until use. For benchmark formulations, SM-102 LNPs were prepared using SM-102: cholesterol: helper lipid: DMG-PEG2000 at a molar ratio of 50:38.5:10:1.5 (N/p = 5.67). ALC-0315 LNPs were prepared using ALC-0315: cholesterol: helper lipid: ALC-0159 at a molar ratio of 47.5:40.7:10:1.8 (N/p = 6.0). Across all formulations, the total lipid-to-mRNA mass ratio was maintained within the range of approximately 19–24 mg total lipid per mg mRNA, depending on ionizable lipid and the helper lipid chemistry and the formulation composition.

4.3 | Particle Size and Zeta Potential

The particle size, polydispersity index (PDI), and zeta potential of the LNPs were characterized using a Dynamic Light Scattering (DLS) Zetasizer (Malvern, UK). The particle size was measured as the intensity-weighted mean hydrodynamic diameter. Unless otherwise specified, zeta potential measurements shown in Figure S2e-h were performed in 1 mM KCl. Additional measurements in 0.1× PBS are presented in Figure S2i to assess surface charge under more physiologically relevant ionic conditions.

mRNA encapsulation

The Quant-iT RiboGreen RNA Assay Kit (Invitrogen) was used to assess mRNA encapsulation efficiency following the manufacturer's instructions. The mRNA encapsulation efficiency (EE) was calculated using the following equation:

$$\text{Encapsulation Efficiency (EE)}(\%) = \frac{\text{Total mRNA (mg/mL)} - \text{Free mRNA (mg/mL)}}{\text{Total mRNA (mg/mL)}} \times 100$$

4.4 | TNS Assay for Apparent pKa

The apparent acid dissociation constant (pKa) of each LNP formulation was evaluated using the fluorogenic probe: 6-(p-toluidino)-2-naphthalenesulfonic acid sodium salt (TNS). Briefly, LNP formulations were added to a series of TNS buffers with pH values ranging from 3.0 to 9.0. The TNS solution in DMSO was incubated with LNPs in buffers at different pH values. The fluorescence intensity was recorded at excitation and emission wavelengths of 320 nm and 430 nm, respectively, using a spectrophotometer. The half-maximal inhibitory pH level (IC50) of the titration curve was reported as the apparent pKa of the LNPs [40].

4.5 | Laurdan Assay

Laurdan dye (6-Dodecanoyl-2-Dimethylaminonaphthalene; Invitrogen) was dissolved at 0.2 mg•mL^{-1} in DMSO and further diluted to 508 µM in 300 mM citrate-phosphate buffer (Boston Bioproducts) at each desired pH values. Separately, LNP formulations were diluted to approximately 3.12 mM total lipid in 10% trehalose solution. For each pH point, 157 µL of diluted Laurdan dye in buffer was pipetted into three replicate wells in a 96-well plate, followed by the addition of 43 µL of diluted LNPs, and mixed by pipetting. Plates were incubated at room temperature for 3 h, after which fluorescence was measured on a SpectraMax M5 microplate reader (Molecular Devices, San Jose, CA). Fluorescence emissions spectra were recorded from 400–600 nm (10 nm increments) using an excitation wavelength of 340 nm. GP values were calculated using the following equation: $GP = (I_{440} - I_{490})/(I_{440} + I_{490})$ [41].

15214095, 0, Downloaded from https://advanced.onlinelibrary.wiley.com/doi/10.1002/adma.75746, Wiley Online Library on [17/11/2026]. See the Terms and Conditions (https://onlinelibrary.wiley.com/terms-and-conditions) on Wiley Online Library for rules of use; OA articles are governed by the applicable Creative Commons License

4.6 | Quartz Crystal Microbalance With Dissipation (QCM-D)

Quartz Crystal Microbalance with Dissipation (QCM-D, QSense Pro, Biolin Scientific) was used to measure the binding of apolipoprotein E (ApoE) to LNPs. Gold-coated QCM-D sensors (QSX301, Biolin Scientific) with a fundamental resonance frequency of 4.95 MHz were initially cleaned in a solution of water, ammonium hydroxide (25%), and hydrogen peroxide (30%) (5:1:1, v/v/v) at 75°C for 5 min. Following adequate rinsing with water, the sensors were dried under nitrogen and subjected to UV/ozone cleaning for 10 min. The sensors were then installed in the flow module of QSense Pro (Q-Sense Inc., Gothenburg, Sweden). Shifts in resonance frequency (ΔF) and dissipation (ΔD) for odd overtones ($n = 1, 3, \ldots, 13$) were recorded. All solutions were introduced using a peristaltic pump (IPC N-4, Ismatec). Experiments were performed at 37°C. ApoE was deposited onto the sensors by injecting 0.1 mg/mL ApoE in PBS at 30 µL/min. After 20 min of adsorption, the surface was rinsed with PBS at 40 µL/min until equilibrium was reached (approximately 10 min). Interactions between the LNP formulations and ApoE were investigated by flowing 50 µg/mL LNPs in PBS over the ApoE-coated surface at a flow rate of 40 µL/min for 90 min. PBS buffer was continuously pumped over the surfaces afterwards.

4.7 | Cryogenic Transmission Electron Microscopy (Cryo-TEM)

LNP formulations were buffer-exchanged into nuclease-free water (Millipore Sigma), vitrified by plunge-freezing, and imaged using brightfield cryo-transmission electron microscopy. TEM grids (Quantifoil GmbH) were glow-discharged for 25 s in rarefied air using a Pelco EasiGlow (Ted Pella). Samples were applied using a Vitrobot Mk IV system (ThermoFisher) at 95% relative humidity and 22°C, blotted, and then plunged into liquid ethane for vitrification. Each sample was vitrified on Quantifoil R2/1 200 mesh grids with and without a 2 nm continuous carbon film. Imaging was performed either on a Talos Arctica TEM (FEI Company) with a K2 direct electron detector (Gatan) controlled by SerialEM software [42] at 49,000× and 130,000× nominal magnification, or on a Tundra TEM (ThermoFisher) controlled by EPU software at 69,000× and 110,000× nominal magnification. Images were collected from grids showing optimal ice thickness and low contamination. Regions of interest exhibiting supramolecular structures were identified.

4.8 | Fourier Analysis

Regions of interest within individual particles were selected and processed using FIJI/ImageJ. Fast Fourier transform (FFT) and d-spacing determination were conducted using the Fiji distribution of ImageJ. A FFT was applied to the regions of interest to reveal periodic structural features. Frequency components corresponding to noise or undesired spatial frequencies were selectively masked to enhance lattice-related signals. An inverse FFT was then computed to reconstruct the spatial domain image emphasizing ordered structures. This approach enables visualization of local crystalline or lamellar organization within the LNP core that may not be apparent in the raw micrograph due to low contrast or overlapping densities.

4.9 | Small-Angle X-Ray Scattering (SAXS)

Small-angle x-ray scattering (SAXS) measurements were performed to evaluate the internal nanostructure of LNP formulations across different pH conditions. Experiments were conducted using a Xeuss 3.0 SAXS/WAXS instrument equipped with a Cu Kα radiation source ($\lambda = 1.5418$ Å) and an Eiger 1 M detector. Samples were analyzed at 25°C using an automated sample-loading system. Two-dimensional scattering patterns were converted to one-dimensional intensity profiles through azimuthal integration, followed by background subtraction using the corresponding buffer controls. Formulations were equilibrated to room temperature prior to analysis.

Quantitative analysis of scattering profiles was performed using Lorentzian peak deconvolution to resolve overlapping structural features. Fitted peak center positions, full-width-at-half-maximum values, and integrated peak areas were subsequently used to compare nanoscale organization and pH-dependent structural transitions across formulations.

$$I(q) = I_0 + \frac{2A_1}{\pi} \cdot \frac{w_1}{4\left(q - q_{c1}\right)^2 + {w_1}^2} + \frac{2A_2}{\pi} \cdot \frac{w_2}{4\left(q - q_{c2}\right)^2 + {w_2}^2}$$

Peak center positions (qc), full width at half maximum (FWHM), and integrated peak areas were extracted from the fitted functions and used for comparative analysis of phase contributions among formulations.

4.10 | Asymmetric Flow Field-Flow Fractionation Coupled With Multi-Angle Light Scattering, Dynamic Light Scattering, and a Differential Refractometer (AF4-MALS-DLS-dRI)

An Agilent 1260 Infinity II HPLC system was coupled to an in-line AF4-MALS-DLS-dRI system. The system comprised an Eclipse Long Channel fitted with a 10kDA regenerated cellulose membrane and a 400 µm laminated spacer. The in-line detectors included a DAWN MALS instrument integrated with WyattQELS dynamic light scattering and an Optilab differential refractometer. For all samples, the dn/dc value was set to 0.16 mL/g and the mobile phase refractive index to 1.331. Baselines from blank runs were subtracted from all samples. Band broadening and delay volumes between detectors were determined using bovine serum albumin (BSA). 5 µL of LNPs at an mRNA concentrations of 0.5 mg/mL were injected onto the Eclipse Long Channel. The channel flow was set to 1.0 mL/min, the injection flow to 0.20 mL/min, and the detector flow to 0.50 mL/min, using 1X PBS as the mobile phase. The focusing position was set to 13%, with focusing performed for 5 min utilizing a crossflow of 0.75 mL/min. Elution was carried out with an initial crossflow of 1.0 mL/min, which decreased exponentially over 40 min to 0.5 mL/min.

15214095, 0, Downloaded from https://advanced.onlinelibrary.wiley.com/doi/10.1002/adma.75746, Wiley Online Library on [17/11/2026]. See the Terms and Conditions (https://onlinelibrary.wiley.com/terms-and-conditions) on Wiley Online Library for rules of use; OA articles are governed by the applicable Creative Commons License

4.11 | Lipid Fusion FRET Assay

Endosome membrane mimicking vesicles were prepared by mixing DOPC, DOPE, NBD-PE, N-Rh-PE, and DOPS (molar ratio 25: 48:1:1:25) in chloroform followed by 1 h under vacuum to form a thin film. The film was further incubated in a vacuum desiccator overnight at room temperature to remove residual chloroform. The following day, the lipid film was resuspended in PBS (pH 7.4) to a final lipid concentration of 1 mM. The mixture was vortexed vigorously to ensure complete detachment of the lipid film from the walls of the round-bottom flask (RBF). The suspension was sonicated for 20 min in a water bath (10 s sonication, 20 s rest) followed by sequential extrusion through 0.2 μm and 0.1 μm polycarbonate membranes (7 passes each). The resulting vesicles exhibited an average hydrodynamic diameter of approximately 140 nm with a PDI < 0.1 as measured by dynamic light scattering.

In a black, clear bottom 96-well plate, 99 μL of PBS at pH 5.5 was added per well. Next, 1 μL of 1 mM liposomes and 10 μl of 1 mM LNP ($n = 3$ per formulation) were added per well, corresponding to a 1:10 liposome:LNP ratio by concentration. The control for minimal fluorescence included wells without LNPs (F_{min}); and the control for maximum fluorescence (Fmax) was treated with 10 μL of 2% Triton X-100. Plates were incubated at 37°C for 5, 15, 30, 45, 60, and 90 min. Fluorescence was measured using a plate reader (λ-excitation = 465 nm, and λ-emission = 520 nm). Lipid fusion was calculated as $(F_{sample} - F_{min})/(F_{max} - F_{min}) * 100$.

4.12 | Primary Cells

Human peripheral blood-derived immature dendritic cells (hDCs; STEMCELL Technologies, Cat. No. 200–0370) were thawed and transferred into pre-warmed RPMI medium supplemented with 10% heat-inactivated FBS and 1% penicillin–streptomycin. Cells were rested at 37°C for 3–4 h, pelleted at 500 × g for 5 min, and resuspended in fresh RPMI at 1×10^6 viable cells/mL. hDCs were seeded at 50,000 cells per well in Phenoplates and incubated at 37°C for 24 h. After 24 h, the medium was replaced with fresh medium prior to transfection for downstream smFISH or immunofluorescence imaging.

4.13 | Single-Molecule Fluorescence In Situ Hybridization (smFISH)

At 24 h post seeding, cells were transfected with 1 μg mRNA/million cells for 4 h. Cells were then washed twice with 1x PBS + 2 mM RNase inhibitor (Ribonucleoside Vanadyl Complex, New England Biolabs, Cat. No. S1402S). All buffers used in smFISH included 2 mM VRC inhibitor to prevent RNA degradation. Cells were fixed and permeabilized using cold (-20°C) 100% methanol at RT for 15 min, followed by washing with 1xPBS twice. Cells were incubated with 1x smFISH wash buffer (2x SSC, 1 mM VRC, 10% deionized formamide) for 30 min. mRNAs were stained with 100 nM custom-designed Stellaris smFISH probe set labeled with Quasar 670 targeting H3 HA mRNA in 1x Stellaris hybridization buffer overnight in a humid incubator at 37°C with shaking. After hybridization, cells were washed twice with 1x wash buffer, for 30 min at 37°C. During the second wash, DAPI (1 ng/μL) was added for nuclear staining. Cells were then washed twice with 1x imaging buffer (2x SSC + 2 mM VRC). Imaging was performed using a Revvity Opera Phenix spinning-disk confocal microscope with a 63x water-immersion objective (NA 1.15). Five z-stacks were acquired with 500 ms exposure per stack. Maximum intensity projected (MIP) images were used for spot identification in Harmony imaging software, with 8 fields of view per well analyzed to quantify total mRNA uptake per cell.

4.14 | Immunofluorescence Imaging

At 24 h after seeding, hDC cells were transfected in fresh media with mRNA-LNPs encoding influenza hemagglutinin (HA H3, Tasmania) at a dose of 10 μg/million cells. After 24 h, cells were washed twice with 1x PBS (no magnesium and calcium), fixed with 4% paraformaldehyde in 1x PBS for 10 min at room temperature, and washed three times with 1x PBS. Cells were blocked with 2% BSA in 1x PBS for 1 h at RT, then stained with a 1:250 dilution of Alexa Fluor 647-labeled anti-H3 antibody (Sanofi stock: 1 mg/mL) and DAPI for 1 h at RT in 1x PBS+0.2% BSA. After washing with 1x PBS + 0.2% BSA thrice for 1 min, cells were imaged in 1x PBS using a Revvity Opera Phenix spinning-disk confocal microscope with a 20x water-immersion objective (NA 1.0) and z-stacks were collected. MIP images were used for quantification of protein expression as mean fluorescence intensity (MFI) from four fields per well using the Harmony imaging software

4.15 | Animal Studies

Ethics statement: Animal studies were conducted in compliance with all relevant US National Institutes of Health regulations, as well as applicable local, state, and federal requirements. Experimental protocols were approved by the Institutional Animal Care and Use Committees (IACUCs) of Alpha Preclinical (North Grafton, MA), Bioqual (Rockville, MD), and New Iberia Research Center (New Iberia, LA). All animal studies at Alpha Preclinical were conducted in accordance with protocols approved by the Alpha Preclinical Institutional Animal Care and Use Committee (IACUC), under protocol number IPF25-01. All animal studies were conducted in accordance with protocols approved by the Tufts University Institutional Animal Care and Use Committee (IACUC), under protocol number G2023-47: *Comprehensive pharmacokinetic (PK) and pharmacodynamics (PD) evaluation of test materials in mice and rats*. All procedures were performed in compliance with applicable Tufts University institutional guidelines and regulations governing the ethical care and use of laboratory animals.

4.16 | Mouse Studies

Animal protocols were approved by the Institutional Animal Care and Use Committee (IACUC). LNPs containing 0.1 μg of hEPO mRNA was intramuscularly injected into the right gastrocnemius muscle of female BALB/c mice (6-8 weeks old). Six hours post-injection, blood samples were collected, and serum hEPO levels were quantified using enzyme-linked immunosorbent assay (ELISA), following the manufacturer's instructions.

15214095, 0, Downloaded from https://advanced.onlinelibrary.wiley.com/doi/10.1002/adma.75746, Wiley Online Library on [17/11/2026]. See the Terms and Conditions (https://onlinelibrary.wiley.com/terms-and-conditions) on Wiley Online Library for rules of use; OA articles are governed by the applicable Creative Commons License

Animals were maintained under pathogen-free conditions with a 12-hour light/dark cycle and ad libitum access to food and water. Test materials were administered as single intravenous doses (5 mL/kg) via tail vein on Day 1. Animals were euthanized 24 h post-dose using carbon dioxide asphyxiation followed by thoracotomy. Terminal blood collection was performed via cardiac puncture using serum separator tubes. For ammonia challenge studies (Days 15 and 22), fasted animals received intraperitoneal injections of freshly prepared 0.2 M ammonium chloride (25 mL/kg). Blood samples were collected via tail vein 30 min post-injection. Serum was extracted from whole blood and stored at -70°C for subsequent ALT/AST analysis by ELISA. Following euthanasia, the liver and spleen were harvested, and 3–6 liver biopsies (4 or 8 mm punches) were collected per animal. Tissue samples were snap-frozen in liquid nitrogen and stored at -70°C for subsequent hOTC quantification by ELISA.

For biodistribution studies, LNPs encapsulating FFLuc mRNA were administered intravenously to male CD1 mice (6-8 weeks old) at a dose of about 0.017 mg/ kg. On Day 2, animals were imaged with an IVIS, with whole body imaging performed 10–15 min after D-Luciferin administration. Animals received 0.2 mL of 15 mg/mL D-luciferin solution via subcutaneous (SC) injection. Animals were anesthetized with isoflurane and positioned in dorsal recumbency (face-up) during imaging. Following euthanasia, the heart, lungs, liver, kidney, and spleen were collected, placed on a single petri dish per group, and subjected to ex vivo IVIS imaging for luminescence.

4.17 | hOTC Studies in Mice

$OTC^{spf\text{-}ash}$ males (4-8 weeks, Jackson Laboratories) were used. Test materials were administered as a single IV dose (5 mL/kg) via tail vein on Day 1. For ammonia challenge studies (Day 2), fasted animals received intraperitoneal injections of freshly prepared 0.2 M ammonium chloride (25 mL/kg). Blood samples were collected via tail vein 30 min post-injection. Animals were euthanized by carbon dioxide asphyxiation followed by thoracotomy. Terminal blood collection was performed via cardiac puncture using serum separator tubes.

Serum was extracted from whole blood and stored at -70°C for subsequent ALT/AST analysis by ELISA. The liver and spleen were harvested, and 3–6 liver biopsies (4 or 8 mm punches) were collected per animal. Tissue samples were snap-frozen in liquid nitrogen and stored at -70°C for hOTC quantification.

For immunogenicity studies, groups of 8 female Balb/c mice (*Mus musculus*) per treatment group were immunized under isoflurane anesthesia with 0.4 µg of HA mRNA in a volume of 0.05 mL of LNP formulation or diluent, administered via the IM route in the quadriceps, on Day 0 (one hind leg) and Day 28 (contralateral leg).

4.18 | Hemagglutination Inhibition (HAI) Assay

HAI assays were performed as previously described [43], using virus stocks A/Tasmania/503/2020 produced in embryonated chicken eggs (Microbiologics). Receptor destroying enzyme (RDE; Fisher Scientific cat # YCC340-122) was used to treat serum samples at a 1:3 serum: RDE ratio, followed by overnight incubation at 37 °C. RDE was then inactivated by incubation at 56 °C for 30 min. Samples were adjusted to a final dilution of 1/10 by the addition of 6 parts 0.5% turkey red blood cells (tRBCs) (Lampire Biological Labs). After a 45 min incubation at room temperature, samples were centrifuged to pellet the tRBCs, and supernatants were transferred to fresh tubes.

HAI assays were performed in V-bottom 96-well plates (BD Falcon cat # 353263). Briefly, 25 µL of RDE-treated, twofold serially diluted serum was mixed with 25 µL of virus (4 hemagglutination units per 25 µL). Subsequently, 50 µL of tRBCs was added, and plates were incubated for 1 h at room temperature. The HAI titer was defined as the highest serum dilution that completely inhibited hemagglutination.

4.19 | MIMIC (Modular IMmune In Vitro Construct) Studies

4.19.1 | PBMC Preparation

Apheresis blood products were collected from donors at a OneBlood blood center (Orlando, FL, USA). The study protocol and donor program were reviewed and approved by Advarra Institutional Review Board (CIRBI Protocol 0906009). Informed consent was obtained from each subject prior to enrollment. Peripheral blood mononuclear cells (PBMCs) from 5 female and 5 male healthy donors aged 18–60 were enriched by Ficoll density gradient separation and cryopreserved in DMSO-containing freezing media according to standard laboratory procedures.

4.19.2 | MIMIC PTE Assay

The MIMIC PTE construct was assembled on a robotic line using previously published methods. Briefly, the human endothelial cell line EA.hy926 (ATCC, Manassas, VA, USA) was grown to confluence on a collagen matrix (Advanced Biomatrix, San Diego, CA, USA). Thereafter PBMCs, prepared from frozen stocks, were added to each well supplemented with heterologous human sera and serum-free media and applied to the endothelial cells in triplicate. After 22 h of incubation with the indicated treatments, cells and supernatant were harvested for downstream assessment. Concentrations of cytokines and chemokines in supernatants were measured using Luminex technology (Austin, TX, USA), while cellular phenotypes and antigen expression were assessed by flow cytometry.

4.19.3 | Cytokine/Chemokine Analysis

MIMIC culture supernatants were analyzed using subsets of the MILLIPLEX Human Cytokine/Chemokine/Growth Factor Panel A (HCYTA-60K) and Panel B (HCYTB-60K) (MilliporeSigma, Burlington, MA, USA), following the manufacturer's protocol, and data were acquired on Luminex xMAP INTELLIFLEX RUO instruments (Austin, TX, USA). Analyte concentrations were calculated based on standard curves using the Bio-Plex Manager software version 6.2 (Bio-Rad, Hercules, CA, USA).

15214095, 0, Downloaded from https://advanced.onlinelibrary.wiley.com/doi/10.1002/adma.75746, Wiley Online Library on [17/11/2026]. See the Terms and Conditions (https://onlinelibrary.wiley.com/terms-and-conditions) on Wiley Online Library for rules of use; OA articles are governed by the applicable Creative Commons License

4.19.4 | Spectral Flow Cytometry

MIMIC PTE-derived PBMCs were harvested and washed with PBS. Cells were stained with Zombie NIR viability dye (BioLegend, San Diego, CA. USA), after which they were fixed in 1% paraformaldehyde, permeabilized with Cytofix/Cytoperm (BD Biosciences), blocked with IgG-Fc (Jackson Immuno Research Laboratories), and stained with the following panel of antibodies diluted in Perm/Wash buffer: Flu H3 HA, CD3, CD4, CD8, CD11c, CD14, CD16, CD19, CD56, and HLA-DR. Data were acquired on a Cytek Aurora spectral flow cytometer and analyzed as described below.

4.19.5 | Statistical Analyses and Data Visualization

Cytokine data were exported to GraphPad Prism 10 (GraphPad Software, San Diego, CA, USA) for visualization. Statistical comparisons between formulations were performed using a paired t test on the log-transformed cytokine concentration values (pg/mL). Statistical significance was represented as ns: $p > 0.05$; *: $p < 0.05$; **, $p < 0.01$; ***: $p < 0.001$; and ****: $p < 0.0001$. Fold changes were calculated using the average of Mock-subtracted concentration values. Flow cytometry data were analyzed using FlowJo v. 10.10.0 (BD, Franklin Lake, NJ, USA) and the OMIQ cloud software suite (Dotmatics, Boston, MA, USA).

4.19.6 | MIMIC B Cell LTE Assay

The methodology for assessing antibody responses in the MIMIC system has been previously described. In summary, adaptive immune responses were evaluated using differentiated antigen-presenting cells (APCs) and isolated B cells, which were either untreated or primed with mRNA-LNPs encoding A/Tasmania/503/2020 HA antigen. Following antigen priming, APCs and B cells were co-cultured with autologous CD4+ T cells for 14 days. Culture supernatants were subsequently collected and analyzed for HA-specific IgG antibodies.

4.19.7 | Antibody Forensics

Antigen-specific IgG was analyzed by Luminex-like magnetic bead-based assay. The protocol involved activating fluorescent labelled magnetic beads and coating them with recombinant A/Tasmania/503/2020 HA protein. Following antigen coating, beads were incubated with MIMIC culture supernatants and subsequently acquired and analyzed using the Bioplex-100 system.

4.19.8 | Statistics

Statistical analyses were conducted using GraphPad Prism version 10.2.3. Differences among group means were assessed using one-way analysis of variance (ANOVA). When the ANOVA indicated a significant effect ($p < 0.05$), post hoc multiple comparisons against the control group were performed using Dunnett's test, which controls the family-wise error rate for multiple comparisons to a single reference group.

4.19.9 | MRNA-LNP Stability

To evaluate the stability of mRNA-LNPs, formulations at 1 mg/mL were aliquoted into sealed glass vials and stored at 4 ^{0}C and 25 ^{0}C, respectively. At predetermined time points, samples were analyzed for a panel of critical quality attributes, including particle size and PDI, mRNA encapsulation efficacy, and mRNA integrity. For mRNA integrity assessment, mRNA was extracted using a Qiagen RNA extraction kit according to the manufacturer's instructions. Integrity (%) was then measured by capillary electrophoresis using a Fragment Analyzer (Agilent Technologies) and analyzed with PROSize 2.0 Software (Agilent Technologies).

4.19.10 | Molecular Dynamics Simulations

MDs simulations were performed to investigate LNP self-assembly and membrane fusion. Self-assembly simulations with varying helper lipid compositions were carried out using GROMACS 2021.6. Membrane fusion simulations employed a modified version of GROMACS 2021.6 [44] that implements a chain reaction coordinate [45, 46] . Potentials of mean force (PMFs) along the fusion pathway were computed using umbrella sampling. All simulations utilized the Martini coarse-grained force field (version 3). Detailed simulation protocols, parameters, analysis methods, and representative simulation movies are provided in the Supporting Information.

Author Contributions

The manuscript was written through contributions of all authors. All authors have given approval to the final version of the manuscript. **Shrirang Karve**: conceptualization, methodology, investigation, writing – original draft, review & editing, visualization, supervision, project administration. **Neha Kaushal**: conceptualization, methodology, investigation, writing – original, review & editing, visualization. **Hanming Zhang**: experimental. **Chetan S. Poojari**: methodology (computational simulations), investigation (computational), formal analysis, writing – original draft (computational sections and si), review & editing. **Dipen Parande**: experimental. **Saket Dolare**: experimental. **Lingyun Liu**: experimental, review and editing. **Zhongyu Li**: experimental. **Trent Northen**: experimental. **Jackie Tang**: experimental. **Jae-Heon Kim**: experimental. **Mengwei Sun**: experimental. **Ana Kume**: experimental. **Krishna Chaitanya Suddala**: experimental, review and editing. **Chung Li Wu**: experimental, data analysis. **Allison Dauner**: experimental, review and editing. **Danielle McCulley**: experimental. **Alex Shumate**: experimental. **David Forgacs**: experimental, review and editing. **Ranjitha Uppala**: experimental. **Jose Salvatico**: experimental. **Rose Jolicoeur**: experimental. **Heesik Yoon**: experimental, review and editing. **Ramesh Dasari**: experimental, **Saswata Karmakar**: experimental **Zhen Hu**: experimental. **Ashish Sarode**: review and editing. **Amita Vaidya**: critical review and editing, graphical abstract. **Younan Ma**: experimental. **Aurélie Deliot**: review and editing. **Solene Bechelli**: data analysis, review & editing. **Michael Rieger**: project administration. **Anusha Dias**: review and editing. **Sudha Chivukula**: review and editing. **Brian Schanen**: review and editing. **Hongfeng Deng**: conceptualization, review and editing, project administration **Frank DeRosa**: writing – review & editing, project administration. **Regis Gervier**: writing – review & editing, project administration.

15214095, 0, Downloaded from https://advanced.onlinelibrary.wiley.com/doi/10.1002/adma.75746, Wiley Online Library on [17/11/2026]. See the Terms and Conditions (https://onlinelibrary.wiley.com/terms-and-conditions) on Wiley Online Library for rules of use; OA articles are governed by the applicable Creative Commons License

Acknowledgements

The authors would like to thank Dr. Hui Wei and Prof. Jason Kaelber from the RCNF at Rutgers University for the Cryo-TEM images. The authors thank Dr. Yiliang Zhang, Dr. Weishi Miao, and Dr. Paul Blundell (Organix, a Symeres Company) for lipid synthesis and insightful discussions. The authors would like to acknowledge Dr. Peter Mikochik (Sanofi) from chemistry group for insightful discussions and Angela Demske, Angkana Baxter, Courtney Caster, Bryce Willis, and John Escobar (Sanofi) for MIMIC experiments. All figure schematics were created using BioRender.com. The authors would like to acknowledge Zon Weng Lai and Fengmei Hua (Sanofi) for HR Mass data acquisition and analysis. The authors are grateful to Dr. Barak Yahalom (Alpha Preclinical) for his contributions to the research presented in this article, and to Jean-Sébastien Bolduc, Kumar Namdev and Gregory Troiano (Sanofi) for reviewing and proofreading the manuscript.

Funding

The research included in the manuscript was funded by Sanofi.

Ethics Statement

All animal studies were conducted at Alpha Preclinical (North Grafton, MA) in accordance with US National Institutes of Health guidelines and relevant local, state, and federal regulations. Experimental protocols were approved by Tufts University's Institutional Animal Care and Use Committee (IACUC) and adhered to ethical guidelines for animal research.

Conflicts of Interest

The authors declare the following financial interests/personal relationships which may be considered as potential competing interests: All the authors are current employees of Sanofi and may hold stock of the company.

Data Availability Statement

The data that support the findings of this study are available from the corresponding author upon reasonable request.

References

1. U. Sahin and K. Karikó, "Türeci, mRNA-Based Therapeutics — Developing a New Class of Drugs," *Nature Reviews Drug Discovery* 13 (2014): 759–780, https://doi.org/10.1038/nrd4278.

2. X. Hou, T. Zaks, R. Langer, and Y. Dong, "Lipid Nanoparticles for mRNA Delivery," *Nature Reviews Materials* 6 (2021): 1078–1094, https://doi.org/10.1038/s41578-021-00358-0.

3. M. Verma, I. Ozer, W. Xie, R. Gallagher, A. Teixeira, and M. Choy, "The Landscape for Lipid-nanoparticle-based Genomic Medicines," *Nature Reviews Drug Discovery* 22 (2023): 349–350, https://doi.org/10.1038/d41573-023-00002-2.

4. E. Kon, N. Ad-El, I. Hazan-Halevy, L. Stotsky-Oterin, and D. Peer, "Targeting Cancer With mRNA–Lipid Nanoparticles: Key Considerations and Future Prospects," *Nature Reviews Clinical Oncology* 20 (2023): 739–754, https://doi.org/10.1038/s41571-023-00811-9.

5. R. Tenchov, R. Bird, A. E. Curtze, and Q. Zhou, "Lipid Nanoparticles-From Liposomes to mRNA Vaccine Delivery, a Landscape of Research Diversity and Advancement," *ACS Nano* 15 (2021): 16982–17015, https://doi.org/10.1021/acsnano.1c04996.

6. C. Wang, Y. Zhang, and Y. Dong, "Lipid Nanoparticle–mRNA Formulations for Therapeutic Applications," *Accounts of Chemical Research* 54 (2021): 4283–4293, https://doi.org/10.1021/acs.accounts.1c00550.

7. J. G. Rurik, I. Tombácz, A. Yadegari, et al., "CAR T Cells Produced in Vivo to Treat Cardiac Injury," *Science* 375 (2022): 91–96, https://doi.org/10.1126/science.abm0594.

8. J. D. Gillmore, et al., "CRISPR-Cas9 in Vivo Gene Editing for Transthyretin Amyloidosis," *New England Journal of Medicine* 385 (2021): 493–502.

9. C. Hald Albertsen, J. A. Kulkarni, D. Witzigmann, M. Lind, K. Petersson, and J. B. Simonsen, "The Role of Lipid Components in Lipid Nanoparticles for Vaccines and Gene Therapy," *Advanced Drug Delivery Reviews* 188 (2022): 114416, https://doi.org/10.1016/j.addr.2022.114416.

10. P. R. Cullis and M. J. Hope, "Lipid Nanoparticle Systems for Enabling Gene Therapies," *Molecular Therapy* 25 (2017): 1467–1475, https://doi.org/10.1016/j.ymthe.2017.03.013.

11. M. Jayaraman, S. M. Ansell, B. L. Mui, et al., "Maximizing the Potency of siRNA Lipid Nanoparticles for Hepatic Gene Silencing in Vivo**," *Angewandte Chemie International Edition* 51 (2012): 8529–8533, https://doi.org/10.1002/anie.201203263.

12. J. Philipp, A. Dabkowska, A. Reiser, et al., "pH-dependent Structural Transitions in Cationic Ionizable Lipid Mesophases Are Critical for Lipid Nanoparticle Function," *Proceedings of the National Academy of Sciences* 120 (2023): 2310491120, https://doi.org/10.1073/pnas.2310491120.

13. Q. Cheng, T. Wei, L. Farbiak, L. T. Johnson, S. A. Dilliard, and D. J. Siegwart, "Selective Organ Targeting (SORT) Nanoparticles for Tissue-Specific mRNA Delivery and CRISPR–Cas Gene Editing," *Nature Nanotechnology* 15 (2020): 313–320, https://doi.org/10.1038/s41565-020-0669-6.

14. K. Paunovska, D. Loughrey, and J. E. Dahlman, "Drug Delivery Systems for RNA Therapeutics," *Nature Reviews Genetics* 23 (2022): 265–280, https://doi.org/10.1038/s41576-021-00439-4.

15. K. Iwakawa, R. Sato, M. Konaka, Y. Yamada, H. Harashima, and Y. Sato, "Cubic Phase-Inducible Zwitterionic Phospholipids Improve the Functional Delivery of mRNA," *Advanced Science* 12 (2025): 2413016, https://doi.org/10.1002/advs.202413016.

16. E. Álvarez-Benedicto, L. Farbiak, M. Márquez Ramírez, et al., "Optimization of Phospholipid Chemistry for Improved Lipid Nanoparticle (LNP) Delivery of Messenger RNA (mRNA)," *Biomaterials Science* 10 (2021): 549–559, https://doi.org/10.1039/D1BM01454D.

17. I. Ermilova and J. Swenson, "DOPC versus DOPE as a Helper Lipid for Gene-therapies: Molecular Dynamics Simulations With DLin-MC3-DMA," *Physical Chemistry Chemical Physics* 22 (2020): 28256–28268, https://doi.org/10.1039/D0CP05111J.

18. J. Iscaro, H. Yu, N. Martinez, et al., "Lyotropic Liquid Crystalline Phase Nanostructure and Cholesterol Enhance Lipid Nanoparticle Mediated mRNA Transfection in Macrophages," *Advanced Functional Materials* 34 (2024): 2405286, https://doi.org/10.1002/adfm.202405286.

19. H. Yu, et al., "Inverse Cubic and Hexagonal Mesophase Evolution Within Ionizable Lipid Nanoparticles Correlates With mRNA Transfection in Macrophages," *Journal of the American Chemical Society* 145 (2023): 24765–24774.

20. D. R. Drake, C. Ortiz, T. Derstepanian et al., "In Vitro Biomimetic Model of the Human Immune System for Predictive Vaccine Assessments," *Disrupt Sci Technol* 1 (2012): 28–40.

21. A. Dauner, P. Agrawal, J. Salvatico, et al., "The in Vitro MIMIC® Platform Reflects Age-Associated Changes in Immunological Responses After Influenza Vaccination," *Vaccine* 35 (2017): 5487–5494, https://doi.org/10.1016/j.vaccine.2017.03.099.

22. L. Wang, H. Morizono, J. Lin, et al., "Preclinical Evaluation of a Clinical Candidate AAV8 Vector for Ornithine Transcarbamylase (OTC) Deficiency Reveals Functional Enzyme From each Persisting Vector Genome," *Molecular Genetics and Metabolism* 105 (2012): 203–211, https://doi.org/10.1016/j.ymgme.2011.10.020.

23. K. Yamazaki, et al., "Lipid Nanoparticle-targeted mRNA Formulation as a Treatment for Ornithine-Transcarbamylase Deficiency Model Mice," *Mol Ther—Nucleic Acids* 33 (2023): 210–226.

15214095, 0, Downloaded from https://advanced.onlinelibrary.wiley.com/doi/10.1002/adma.75746, Wiley Online Library on [17/11/2026]. See the Terms and Conditions (https://onlinelibrary.wiley.com/terms-and-conditions) on Wiley Online Library for rules of use; OA articles are governed by the applicable Creative Commons License

24. A. Sarode, C. Ortiz, T. Derstepanian, et al., "Potent Liver-Tropic mRNA Lipid Nanoparticles: ApoE-Mediated Delivery Through a Low-Density Lipoprotein Receptor Independent Uptake Mechanism," *Advanced Materials* 38 (2025): 17893, https://doi.org/10.1002/adma.202517893.

25. S. Kawamoto and W. Shinoda, "Free Energy Analysis Along the Stalk Mechanism of Membrane Fusion," *Soft Matter* 10 (2014): 3048–3054, https://doi.org/10.1039/c3sm52344f.

26. L. R. Kjølbye, M. Valério, M. Paloncýová, et al., "Martini 3 Building Blocks for Lipid Nanoparticle Design," *Journal of Chemical Theory and Computation* 22 (2026): 1069–1091, https://doi.org/10.1021/acs.jctc.5c01207.

27. R. L. Goldman, N. T. Vittala Murthy, T. P. Northen, et al., "Understanding Structure Activity Relationships of Good HEPES Lipids for Lipid Nanoparticle mRNA Vaccine Applications," *Biomaterials* 301 (2023): 122243, https://doi.org/10.1016/j.biomaterials.2023.122243.

28. L. Liu, J.-H. Kim, Z. Li, et al., "PEGylated Lipid Screening, Composition Optimization, and Structure–activity Relationship Determination for Lipid Nanoparticle-mediated mRNA Delivery," *Nanoscale* 17 (2025): 11329–11344, https://doi.org/10.1039/D5NR00433K.

29. I. M. Hafez and P. R. Cullis, "Roles of Lipid Polymorphism in Intracellular Delivery," *Advanced Drug Delivery Reviews* 47 (2001): 139–148, https://doi.org/10.1016/S0169-409X(01)00103-X.

30. M. Wagner, S. Holzschuh, A. Traeger, A. Fahr, and U. S. Schubert, "Asymmetric Flow Field-Flow Fractionation in the Field of Nanomedicine," *Analytical Chemistry* 86 (2014): 5201–5210.

31. G. Sahay, W. Querbes, C. Alabi, et al., "Efficiency of siRNA Delivery by Lipid Nanoparticles Is Limited by Endocytic Recycling," *Nature Biotechnology* 31 (2013): 653–658, https://doi.org/10.1038/nbt.2614.

32. J. Kim, A. Jozic, Y. Lin, et al., "Engineering Lipid Nanoparticles for Enhanced Intracellular Delivery of mRNA Through Inhalation," *ACS Nano* 16 (2022): 14792–14806, https://doi.org/10.1021/acsnano.2c05647.

33. N. Saber, M. E. Senti, and R. M. Schiffelers, "Lipid Nanoparticles for Nucleic Acid Delivery Beyond the Liver," *Human Gene Therapy* 35 (2024): 617–627, https://doi.org/10.1089/hum.2024.106.

34. L. N. Kasiewicz, S. Biswas, A. Beach, et al., "GalNAc-Lipid Nanoparticles Enable Non-LDLR Dependent Hepatic Delivery of a CRISPR Base Editing Therapy," *Nature Communications* 14 (2023): 2776, https://doi.org/10.1038/s41467-023-37465-1.

35. M. Kim, E. S. Song, J. C. Chen, et al., "Dual SORT LNPs for Multi-Organ Base Editing," *Nature Biotechnology* 44 (2025): 578–586, https://doi.org/10.1038/s41587-025-02675-z.

36. X. Xu and T. Xia, "Recent Advances in Site-Specific Lipid Nanoparticles for mRNA Delivery," *ACS Nanoscience Au* 3 (2023): 192–203, https://doi.org/10.1021/acsnanoscienceau.2c00062.

37. S. Omo-Lamai, Y. Wang, M. N. Patel, et al., "Limiting Endosomal Damage Sensing Reduces Inflammation Triggered by Lipid Nanoparticle Endosomal Escape," *Nature Nanotechnology* 20 (2025): 1285–1297, https://doi.org/10.1038/s41565-025-01974-5.

38. S. J. Marrink, H. J. Risselada, S. Yefimov, D. P. Tieleman, and A. H. Vries, "The MARTINI Force Field: Coarse Grained Model for Biomolecular Simulations," *Journal of Physical Chemistry B* 111 (2007): 7812–7824, https://doi.org/10.1021/jp071097f.

39. C. S. Poojari, K. C. Scherer, and J. S. Hub, "Free Energies of Membrane Stalk Formation From a Lipidomics Perspective," *Nature Communications* 12 (2021): 6594, https://doi.org/10.1038/s41467-021-26924-2.

40. J. Zhang, H. Fan, D. A. Levorse, and L. S. Crocker, "Ionization Behavior of Amino Lipids for siRNA Delivery: Determination of Ionization Constants, SAR, and the Impact of Lipid pK a on Cationic Lipid–Biomembrane Interactions," *Langmuir* 27 (2011): 1907–1914, https://doi.org/10.1021/la104590k.

41. T. Parasassi, G. D. Stasio, G. Ravagnan, R. M. Rusch, and E. Gratton, "Quantitation of Lipid Phases in Phospholipid Vesicles by the Generalized Polarization of Laurdan Fluorescence," *Biophysical Journal* 60 (1991): 179–189, https://doi.org/10.1016/S0006-3495(91)82041-0.

42. D. N. Mastronarde, "Advanced Data Acquisition From Electron Microscopes With SerialEM," *Microscopy and Microanalysis* 24 (2018): 864–865, https://doi.org/10.1017/S1431927618004816.

43. S. Chivukula, et al., "Development of Multivalent mRNA Vaccine Candidates for Seasonal or Pandemic Influenza," *npj Vaccines* 6 (2021): 153.

44. M. J. Abraham, et al., "GROMACS: High Performance Molecular Simulations Through Multi-level Parallelism From Laptops to Supercomputers," *SoftwareX* 1 (2015): 19–25.

45. J. S. Hub and N. Awasthi, "Probing a Continuous Polar Defect: A Reaction Coordinate for Pore Formation in Lipid Membranes," *Journal of Chemical Theory and Computation* 13 (2017): 2352–2366, https://doi.org/10.1021/acs.jctc.7b00106.

46. C. L. Ting, N. Awasthi, M. Müller, and J. S. Hub, "Metastable Prepores in Tension-Free Lipid Bilayers," *Physical Review Letters* 120 (2018): 128103, https://doi.org/10.1103/PhysRevLett.120.128103.

Supporting Information

Additional supporting information can be found online in the Supporting Information section.

Supporting File 1: adma75746-sup-0001-SuppMat.docx.

Supporting File 2: adma75746-sup-0002-SuppMat.docx.

15214095, 0, Downloaded from https://advanced.onlinelibrary.wiley.com/doi/10.1002/adma.75746, Wiley Online Library on [17/11/2026]. See the Terms and Conditions (https://onlinelibrary.wiley.com/terms-and-conditions) on Wiley Online Library for rules of use; OA articles are governed by the applicable Creative Commons License